UNDERSTANDING TWO COUPLED ROTORS

M.Sc. Dissertation Report (IV semester)

Monish B

Roll No. 22025762028

Department of Physics & Astrophysics,
University of Delhi, Delhi - 110007, India.

May 2024

ACKNOWLEDGEMENTS

First and foremost, I extend my heartfelt gratitude to my supervisor, **Dr. Awadhesh Prasad**, Professor, Department of Physics & Astrophysics, University of Delhi, for entrusting me with the task of devising a model for the coupled camphor ribbon system. Additionally, I deeply appreciate **Dr. Sangeeta D. Gadre,** Professor of Physics, Kirori Mal College, University of Delhi, for initiating numerous discussions, providing valuable insights, and clarifying concepts that formed the basis for our modeling endeavors. It is important to acknowledge that the completion of this dissertation and the results presented herein wouldn't have been possible without the collective efforts.

Throughout the semester, our daily discussions gradually built up understanding akin to assembling blocks, with occasional setbacks that were eventually overcome, strengthening our foundation. Working alongside them has not only enriched my understanding of the subject matter but has also imparted invaluable lessons that will continue to guide me in my scientific career. I extend my heartfelt appreciation for their patience in bearing all my delays and unbiased guidance throughout. Additionally, I'm indebted to Dr. Punit Parmananda's lab, IIT-B, for providing experimental videos, which allowed us to stay on track and validate our modeling at each step.

Furthermore, I came to appreciate the significance of user-level interaction in programming, which significantly streamlined our workflow and saved considerable time. This insight prompted me to adopt different approaches and underscored the integral role of programming in scientific research. I am grateful for the clean code base and thorough documentation provided by DynamicalSystems.jl, which facilitated the realization of this goal with minimal effort. Additionally, I extend my thanks to Julia forum and IRC channel #julia for their assistance whenever I encountered challenges.

Given the heavy reliance of this dissertation on computational power, the provision of backup machines was indispensable. I extend my sincere appreciation to my friends Inomik and Muskan for providing access to their *nix machines with setups of Julia-1.9 and LaTeX, which proved invaluable in ensuring continuity and peace of mind in the face of unforeseen events.

Lastly, I owe my current position and achievements to the support of my family. Their trust, encouragement, and assistance have played a huge role in shaping the path that has led me to where I am today.

Monish B

May 2024

DECLARATION

I hereby declare that the work presented in this dissertation entitled UNDERSTANDING TWO COUPLED ROTORS is originally carried out by me independently in the Department of Physics & Astrophysics, University of Delhi, under the supervision of Prof. Awadhesh Prasad. I further declare that this work has not formed the basis for the award of any degree, diploma, fellowship or similar title of any other University or Institution.

May 2024

Monish B

Department of Physics & Astrophysics,
University of Delhi, Delhi - 110007

CERTIFICATE

This is to certify that Mr. Monish B student of M.Sc. Physics, Department of Physics & Astrophysics, University of Delhi has done his dissertation during his IV Semester, January 2024 - May 2024 under my supervision. The work entitled UNDERSTANDING TWO COUPLED ROTORS embodies the original study under taken by Mr. Monish B.

Prof. Awadhesh Prasad

Department of Physics & Astrophysics,
University of Delhi, Delhi - 110007

May 2024

ABSTRACT

In this dissertation, we delve into the intricate dynamics of camphor particles, which serve as prime candidates for the study of active particles due to their controllable nature and adaptability to various experimental setups. We draw parallels between the mechanics of collective behavior of particles and synchronization, both fascinating fields within nonlinear dynamics. Our work revolves around a system that encapsulates these behaviors, divided into several parts for thorough exploration.

Firstly, we lay down the essentials of nonlinear dynamical concepts, providing a theoretical foundation for understanding the system. We then shift focus to camphor ribbons as coupled oscillators, investigating their behavior in detail. Utilizing the Coulomb-Yukawa potential, which exhibits both attractive and repulsive characteristics, we model the camphor ribbon system based on insights gained from experimental videos. Our findings suggest that this potential captures the system's behavior more accurately than the previously proposed Yukawa potential.

Moving forward, we delve into the analytical behavior of the system, determining that the order of the potential should be greater than 2 for stability analysis. We validate our analytical predictions through numerical integration, ensuring consistency between theoretical expectations and computational simulations. Furthermore, we compare our results with previously published synchronization limit conditions, demonstrating alignment with experimental data.

Exploring further, we identify various types of librated motion at specific energy levels, noting a transition to solely co-rotating synchronized motion beyond a certain threshold. Interestingly, we observe that this behavior is consistent across all orders of the Coulomb-Yukawa potential.

Finally, we discuss the tools employed for simulation and conclude with suggestions for further improvements to the model, highlighting avenues for future research and development.

Contents

[1]This section is grounded in the synchronization condition reported by Jain et al. (2023) in Section III, Results and Discussion, page 4.

List of Figures

Chapter 1

Introduction

1.1 Overview

Striving for coherence and self-containment, this chapter revisits vital definitions and concepts from the III semester - 2023 dissertation. The structure unfolds with an initial exploration of analytical tools in nonlinear dynamics. Subsequently, attention shifts to the system's components, focusing on camphor ribbons and their interactions. This is followed by an examination of various forms of interaction potential, accounting the rationale behind the selection of Coulomb-Yukawa type. The subsequent chapter utilizes the analytical techniques introduced earlier to study the modeled potential and a concluding section on synchronization between different rotor states. We now embark on review of fundamentals.

1.2 Dynamical Systems

We focus on preparing the necessary tools and techniques for conducting stability analysis in a dynamical system. Our aim is to provide a comprehensive overview of the linearization techniques employed for analytical studies, drawing insights from Strogatz (2015). By developing these fundamental tools, we pave the way for a thorough examination of the stability characteristics within dynamical systems, offering a solid foundation for subsequent analyses and assessments

Dynamics - Study of change in evolving systems over time and position. Whether a system reaches equilibrium, exhibits cyclic patterns, or displays more intricate patterns, dynamics provides analytical tools for investigation. For instance, instead of tracking the precise positions of planets continuously, questions about the long-term stability of the solar system led Poincaré to develop a geometric approach thus studying 3-body problem. This approach formed the foundation for the subject of dynamics.

Chaos enters the picture when deterministic systems demonstrate aperiodic behavior sensitive to initial conditions, making long-term predictions impossible. In chaotic systems like the atmosphere, small errors in measuring the current state can rapidly amplify, leading to unreliable forecasts. Lorenz (1963)'s groundbreaking work revealed structure within chaos, demonstrating that solutions to his equations formed a butterfly-shaped set of points in three dimensions. This discovery laid the groundwork for the interconnected fields of nonlinear dynamics and chaos.

What's being non-linear?

There are two main types of dynamical systems: differential equations and iterated maps. Differential equations describe the evolution of systems in continuous time, whereas iterated maps arise in problems where time is discrete.

A very general framework for ordinary differential equations is provided by the following system,

$$\begin{aligned}\dot{x}_1 &= f_1(x_1, ..., x_n)\\ &\vdots\\ \dot{x}_n &= f_n(x_1, ..., x_n).\end{aligned} \tag{1.1}$$

Here the overdots denote differentiation with respect to t. $\dot{x}_i = \frac{dx_i}{dt}$, and the functions $f_1, \ldots, f_n$ are determined by the problem at hand. A system is said to be linear, when all the x on the right-hand side appear to the first power only, taking an example of normalized damped harmonic oscillator $\ddot{x} + \dot{x} + x = 0$ and reducing into two 1^{st} order ODEs.

$$\begin{aligned}\dot{x} =& y\\ \dot{y} =& -y - x.\end{aligned} \tag{1.2}$$

An example of non-linear systems would be, driving force F added to above such that $\ddot{x} + \dot{x} + x = F\cos(t)$. Here, $\cos(t)$ expansion involves higher-order polynomials, leading to the classification of the system as non-linear. Further this can be reduced into three 1^{st} order ODEs,

$$\begin{aligned}\dot{x} =& y\\ \dot{y} =& -y - x + F\cos(z)\\ \dot{z} =& 1.\end{aligned}$$

By this reduction, phase space trajectories can be visualized with one of the variables frozen in time, hence observing behaviour of the system becomes possible when analytical solution isn't feasible.

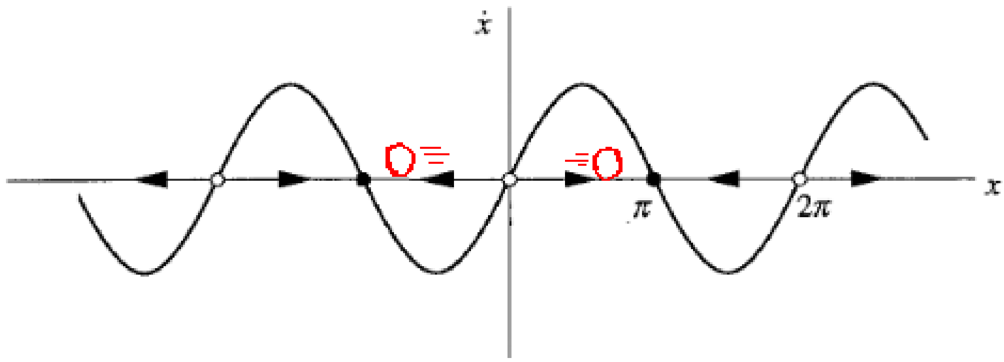

Figure 1.1: Phase portrait of $\dot{x} = \sin(x)$.

1.3 One Dimension Flow $\dot{x} = f(x)$

A single equation of the above form where $x(t)$ is a real-valued function of time t, and $f(x)$ is a smooth real-valued function of x are one-dimensional or first-order systems. As an example,

$$\dot{x} = \sin(x). \tag{1.3}$$

One of the ways to solve is integrating over t and finding a general solution for x, but most of the cases analytical integration may not be straightforward so we seek other techniques to analyze the system.

1.3.1 Geometrical Essence

Making a plot of x vs $\dot{x}$ for Eq. (1.3) and asking how points on the 1-D line evolve will tell us long time behaviour of the system. We start analyzing the system by finding what the **fixed points** are, by setting $\dot{x} = 0$ in Eq. (1.3). The corresponding fixed points are $n\pi$, $n \in \mathbb{Z}$. As an analogy think of placing a ball on a 1-D plank depicted in Fig. 1.1 and it's motion dictated by $\dot{x}$ which can be thought of vector field given by the system, if ball is placed exactly on the fixed point 0 or π light/grey circle shown in Fig. 1.1 it remains fixed without moving. Next is depicting effects of $\dot{x}$ with arrows, it's positive(negative) in the interval $[0,\pi]([\pi,2\pi])$ so a right(left) one. Arrows are shown on x-axis since the system is 1-D. Being equipped with all the necessary details, one can start to analyze how each point evolves. Example, placing a imaginary ball anywhere between $[0,\pi]$, $[\pi,2\pi]$ on the x-axis line will make it move towards π and away from 0. These behaviours are dictated by behaviour of fixed points and there are analytical techniques to classify, we see one such technique in the following section and build the same for N-dimensions.

1.3.2 Fixed Points Behaviour

By setting $\dot{x} = f(x) = 0$, we obtained the fixed points, let these be x^*. These fixed points are characterized by their stability, i.e., when we perturb a little from the fixed point we seek the answer whether they evolve further away or stay close or get back to the fixed point itself, depending upon these they are classified as;

- **Stable fixed point** - perturbation from this point decays over time bringing back to fixed point itself.
- **Unstable fixed point** - perturbation grows over time in both the directions and approaches a stable point.
- **Saddle Point** - perturbation grows in one direction while decays in another.

Now to analytically find out these, one can introduce perturbation term $\eta(t) = x(t) - x^*$, knowing how $\eta(t)$ changes will tell whether perturbation grows or decays which in turn gives information about stability of the system. Taking time derivative of perturbation, we have

$$\begin{aligned} \dot{\eta}(t) =& \frac{d}{dt}(x(t) - x^*) \qquad (1.4)\\ =& f(x^* + \eta) \\ =& f(x^*) + \eta f^{'}(x^*) + O(\eta^2) \\ \dot{\eta} \propto& f^{'}(x^*). \qquad (1.5) \end{aligned}$$

Here $f(x^* + \eta)$ is Taylor expanded around x^*, where $f^{'}(x^*) = \frac{d(f(x))}{dx}|_{x=x^*}$ and $O(\eta^2)$ higher order terms were neglected. This forms the ground work of **Linearization**. We conclude from Eq. (1.5) perturbation growth/decay depends on the slope of $f(x)$ at fixed point and classified as

- $f^{'}(x^*) > 0$ unstable fixed point.
- $f^{'}(x^*) < 0$ stable fixed point since perturbation decays.
- $f^{'}(x^*) = 0$ marginal point, further geometrical analysis is necessary to classify.

Now derivative of Eq. (1.3) is $f^{'}(x) = cos(x)$,

- $f^{'}(0) > 0$ – 0 being unstable fixed point, marked by lighter circle (see Fig. 1.1)
- $f^{'}(\pi) < 0$ - π being stable fixed point.

This analysis aligns with the geometric method discussed earlier, thereby confirming its validity. One of the most reliable methodologies for developing a system model involves identifying fixed points and understanding their behavior through linearization or geometric approaches, and then comparing these results with observed behaviors. However, simplified models often fail to accurately replicate the actual system due to influences from external factors such as temperature, length, concentration, mass, etc. Incorporating these factors as parameters into the model is crucial for obtaining reliable results. The number of parameters to be included depends on the scale and objectives of the study. These parameters significantly influence the qualitative structure of the model, potentially leading to the creation or elimination of fixed points or alterations in their stability. This discussion leads us to the topic of bifurcations.

1.3.3 Bifurcation

A system parameter can significantly impact the system's dynamics, leading to qualitative changes such as the creation or disappearance of fixed points or alterations in their stability. These transformative phenomena are known as bifurcations. Now, we will study the bifurcation with an illustrative example. We introduce a real parameter c into the previously analyzed equation Eq. (1.3)

$$\dot{x} = f(x) = \sin(x) - c. \tag{1.6}$$

Following previous approach, we determine fixed points by setting $\dot{x} = 0$

$$\begin{aligned} 0 &= \sin(x) - c \\ c &= \sin(x) \\ \sin^{-1}(c) &= x. \end{aligned} \tag{1.7}$$

solutions of Eq. (1.3) are fixed points x^* and they varies with parameter c as

$$x^* = \begin{cases} -\sin^{-1}(c) + \pi + 2n\pi \\ \sin^{-1}(c) + 2n\pi. \end{cases} \quad n \in \mathbb{Z} \tag{1.8}$$

Domain of $sin^{-1}(c)$ is $[-1, 1]$ and it tells fixed points vanish when parameter, $|c| > 1$. To picturize these, we plot (see Fig. 1.2) between c vs x^*.

When $c = 0$, Eq. (1.6) simplifies to Eq. (1.5), revealing previously identified fixed points at 0 and π, characterized as unstable and stable, respectively. In Fig. 1.2, for $c = 0$, the vertical axis intersections x^* align with these fixed points, 0 lying on the **dashed line** representing the

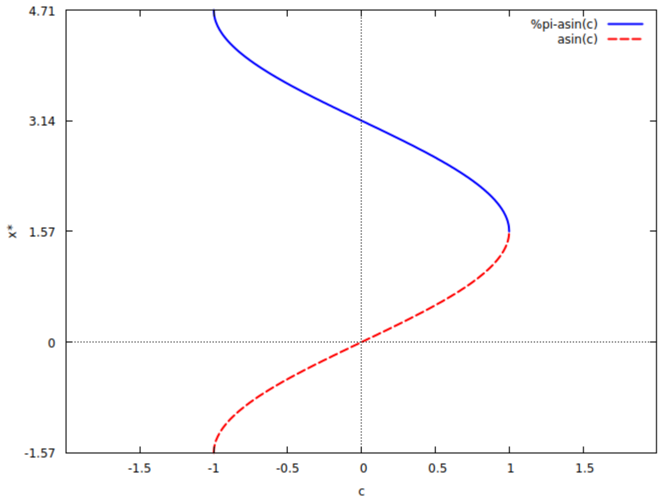

Figure 1.2: Bifurcation plot of Eq. (1.6) satisfying Eq.(1.8).

branch of **unstable** fixed points, and π on the **solid line** representing the branch of **stable** fixed points. The convergence of these two branches occurs at $c = 1$ and $c = -1$, facilitated by the relationship $\frac{3\pi}{2} = 2\pi - \frac{\pi}{2}$. Beyond $|c| > 1$, no intersections occur, resulting in the disappearance of fixed points. This transition marks a bifurcation point, highlighting the dynamic behavior as the system undergoes a qualitative change in its fixed-point structure.

Examining the plots in Figs. 1.1 and Fig. 1.2, a transition to angular phase space simplifies the analysis, providing a more accessible representation. By wrapping the x intervals with a period of 2π, the intricacies of the system become more apparent, and periodicity or cyclicity can be seen with ease. This transition to periodic representation not only enhances our understanding but also allows for a clearer visualization of the cyclic patterns embedded in the system's dynamics.

1.3.4 1-D circular flow

Vector fields on the circle representing rotation with constant radius provide the most basic model of systems that can oscillate which is not possible in 1-D flows where trajectories can only converge to or diverge from fixed points, but in circular flow since it's flowing one direction, a particle can eventually return to its starting place. Form of system in Fig. 1.2 can be written as

$$\dot{\theta} = f(\theta) = \sin(\theta) - c,$$

this represents the same model as Eq. (1.6) but takes periodicity into account, hence bringing out the cyclic pattern, these circular flows form basis for higher dimensional system like coupled rotors studied later.

Now, we will translate the techniques and insights gained from the analysis of one-dimensional systems to the more intricate realm of N-dimensional ones. This transition broadens our analytical toolkit and lays the groundwork for the investigation of coupled systems that exhibit exotic behaviors.

1.4 N-Dimensional Phase Space Analysis

In our exploration of N-dimensional phase space analysis, we initially focus on solving linear systems before delving into the complexities of non-linear systems. For a linear differential equation represented as

$$\dot{\underline{x}} = \underline{f}(\underline{x}) = A\underline{x} \tag{1.9}$$

where $\underline{x}$ is an N-dimensional vector and A is an N-by-N matrix, our goal is to analyze the system by identifying fixed points $\dot{\underline{x}} = 0$ and examining their stability. To solve an arbitrary N-dimensional system described by Eq. (1.9), we introduce an ansatz:

$$\underline{x} = \underline{V}e^{\lambda t}. \tag{1.10}$$

By taking time derivative of this expression and substituting it back into the linear equation Eq. (1.9), we obtain the equation $A\underline{V} = \lambda\underline{V}$ as described below,

$$\begin{aligned}
\dot{\underline{x}} &= \underline{V}\lambda e^{\lambda t} \\
A\underline{x} &= \underline{V}\lambda e^{\lambda t} \\
A\underline{V}e^{\lambda t} &= \underline{V}\lambda e^{\lambda t} \\
A\underline{V} &= \lambda\underline{V}.
\end{aligned} \tag{1.11}$$

Recognizing that $\underline{x} = \underline{V} = \underline{0}$ is always a solution, we impose the condition $det(A - I\lambda) = 0$ to find non-trivial solutions. In essence, for systems like Eq. (1.9), the evolution of phase space trajectories are determined by the eigenvalues and eigenvectors of matrix A.

1.4.1 Generalizing For Non-Linear Systems

Expanding our analysis to non-linear systems, we investigate if the linear results hold similarities. Let (x^*, y^*) be the fixed points of one such 2-D governed by,

$$\begin{aligned}\dot{x} &= f(x,y)\\ \dot{y} &= g(x,y).\end{aligned}$$

Examining small perturbations around fixed points and observing their behavior in the vicinity, we note the similarity to the 1-dimensional case discussed earlier. Specifically, we define $u(t)$ and $v(t)$ as the perturbations around the fixed points x^* and y^*, respectively. This allows us to express the perturbations as:

$$\begin{aligned}u(t) =& x(t) - x^*\\ v(t) =& y(t) - y^*.\end{aligned}$$

To understand how these perturbations evolve over time, we take the time derivative. However at fixed points, $\dot{x^*} = \dot{y^*} = 0$, therefore

$$\begin{aligned}\dot{u} =& \dot{x} = f(x,y) = f(x^* + u, y^* + v),\\ \dot{v} =& \dot{y} = g(x,y) = g(x^* + u, y^* + v).\end{aligned}$$

By Taylor expansion, these equations become:

$$\begin{aligned}\dot{u} =& f(x^*, y^*) + u(t)\frac{\partial f}{\partial x} + v(t)\frac{\partial f}{\partial y} + O(n^2),\\ \dot{v} =& g(x^*, y^*) + u(t)\frac{\partial g}{\partial x} + v(t)\frac{\partial g}{\partial y} + O(n^2).\end{aligned}$$

Neglecting higher-order terms and expressing these equations in matrix form, we get:

$$\begin{aligned}\begin{bmatrix}\dot{u}\\ \dot{v}\end{bmatrix} &= \begin{bmatrix}\frac{\partial f}{\partial x} & \frac{\partial f}{\partial y}\\ \frac{\partial g}{\partial x} & \frac{\partial g}{\partial y}\end{bmatrix}\begin{bmatrix}u\\ v\end{bmatrix}\\ \underline{\dot{u}} &= \mathscr{J}\,\underline{u}.\end{aligned} \tag{1.12}$$

This matrix form resembles Eq. (1.9), allowing us to find eigenvalues and eigenvectors of the Jacobian matrix $\mathscr{J}$. By doing so, we can infer the phase space trajectory behaviors. This linearization technique can be extended to N-dimensions, providing a powerful tool for analyzing the stability of nonlinear systems.

Equipped with various analytical techniques, we will take a detour to explore the system at the center of our study: the coupled rotor system. Initially, we provide details about camphor ribbons and their driving mechanisms. Then examining an experimental setup detailed by Sharma et al. (2019), where two such ribbons interact.

In this context, we modeled the system's coupling potential using a Coulomb-Yukawa-type coupling. Through the application of nonlinear dynamical techniques, we will analyze the fixed points and their stability, shedding light on the rationale behind remodeling from the framework established by previous researchers Sharma et al. (2019, 2020); Jain et al. (2023, 2022). This exploration sets the stage for a comprehensive investigation into the dynamics of coupled rotor systems, offering valuable insights into the reliability of the modeled potential.

Chapter 2

Camphor Rotors

In this chapter, we provide details on the phenomena of camphor motion when dispersed in water, exploring the origin of this **self-propelled motion** and the nature of their coupling when more than one camphor is introduced. Additionally, we glance through different experimental setups of coupled camphor systems before introducing to the camphor ribbons, which we investigate subsequently. This overview in Fig. 2.1 is essential because understanding these intricate dynamics sheds light on increasing complexity of model in further studies.

2.1 What are Camphors?

Camphor is a waxy, white or transparent solid with a strong aroma Mann et al. (1994), obtainable either through the condensation of vapors released during the roasting of wood chips or by synthesizing it from organic compounds Chen et al. (2013). When small scrapings of camphor are dispersed on the surface of water, they exhibit intriguing motion patterns influenced by irregularities in their shape. Numerous studies, including those conducted by Nakata Satoshi & Ose (1997), have explored the self-motion of camphors, revealing their tendency for self-rotation and laying the groundwork for the development of camphor rotors. Building upon this foundation, various experimental setups have been devised to control and manipulate the motion of these rotors, offering valuable insights into the underlying principles.

Expanding our exploration into the realm of camphors, we delve into the intriguing variations that arise when different shapes are introduced. Specifically, we shift our focus to different models which present unique characteristics and behaviors compared to the previously mentioned scrapings. By examining these distinct forms, we aim to unravel additional aspects of camphor dynamics and uncover the specific influences that shape has on their self-motion.

2.2 Self-propulsion Mechanism

Numerous driving mechanisms have been devised for self-propelled objects, with one particularly popular approach based on the **interfacial tension gradient** Suematsu et al. (2014). In systems utilizing this mechanism, the driving force originates from the difference in surface tension around

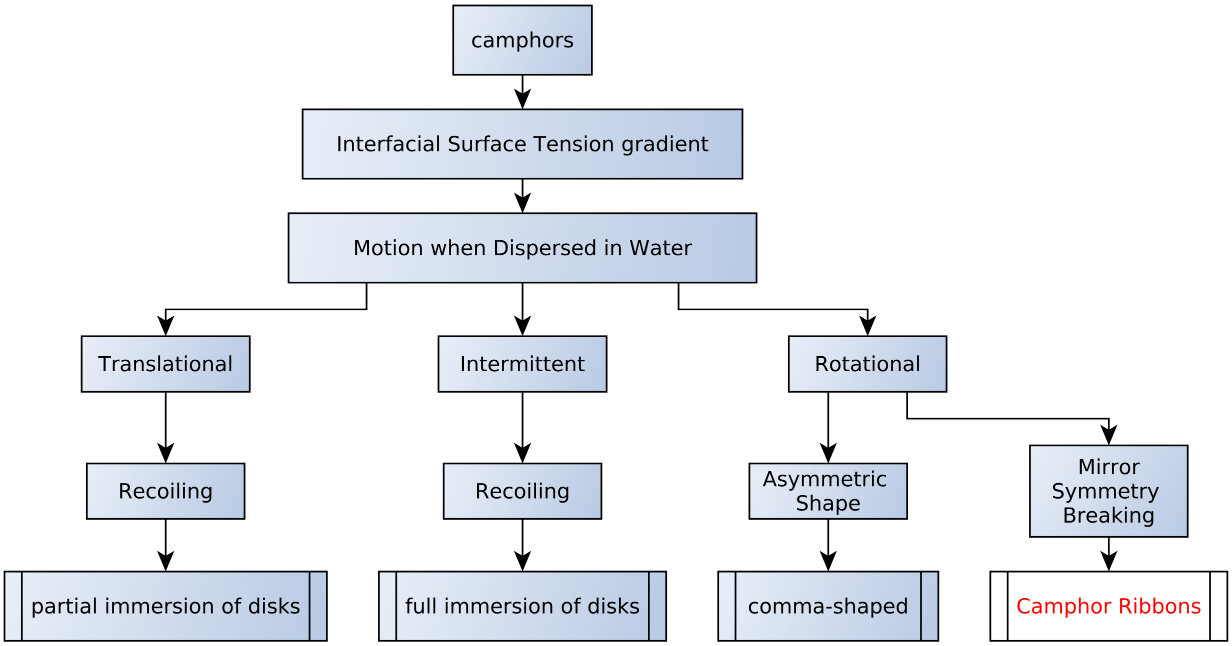

Figure 2.1: A flowchart illustrating camphor-related systems, with end nodes displaying examples of such systems that exhibit all the directed properties outlined above.

the object. This contrast is induced by the dissolution of surfactants released from the object itself, causing the water surface to pull the object towards regions with higher surface tension. This uncomplicated mechanism, commonly referred to as the Marangoni Effect has been verified qualitatively by numerous experiments Nakata Satoshi & Ose (1997) and it's given by,

$$F_m \propto (\gamma_{front} - \gamma_{back}),$$

where F_m represents the pulling force from the water surface and is proportional to the difference in surface tension, $\Delta\gamma$. This phenomenon is influenced by the concentration of solute, driving variations in γ, and temperature, as dissolved camphor layers are volatile.

Additional factors, such as convection Kitahata et al. (2004) and pressure gradient may contribute to the overall explanation. While there might be other elements at play, Marangoni effects seems sufficient to comprehensively elucidate the phenomenon. Now, let's transition to a brief discussion on how these effects become evident in different models, giving rise to various motions.

2.2.1 Translational Motion

In Suematsu et al. (2014) experimental model, camphor disks are strategically positioned on the plastic boat, with only half of each disk projecting over the water, as shown in Fig. 2.2 . This design

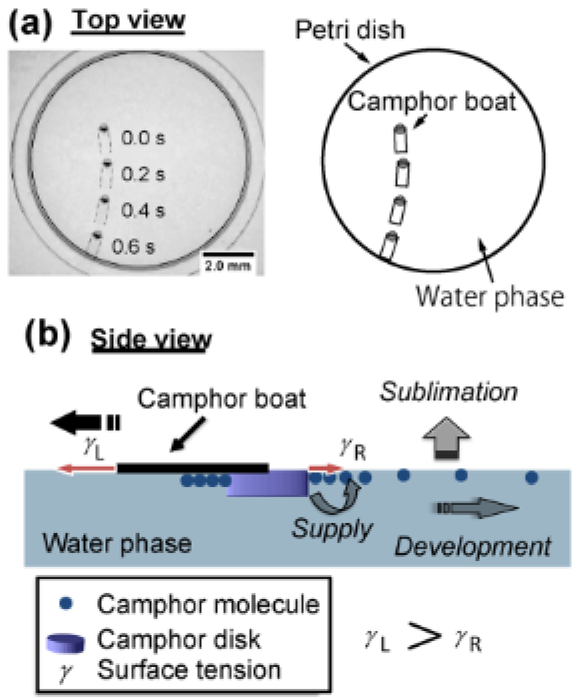

Figure 2. (a) A superimposed image of the self-motion of a camphor boat (left) and its illustration (right). The time interval is 0.2 s. (b) Illustration of the mechanism of self-motion. Camphor molecules are supplied from a camphor disk to the water surface and form a molecular layer. The molecular layer decreases surface tension on the right-hand side of the boat, and the surface tension difference then drives the boat to the left.

Figure 2.2: Self propulsive mechanism of Camphor Boats referenced from Suematsu et al. (2014)

prompts camphor molecules at the back to spontaneously dissolve on the air/water surface, while the plastic at the front obstructs dissolution. This asymmetry results in increased surface tension at the front compared to the back, creating a gradient in interfacial surface tension between dissolved camphor molecules and the water surface. Consequently, the plastic boat is propelled towards higher surface tension or in the direction of less contraction of camphor molecules, explaining its translatory motion.

However, this method has a notable drawback – it fails to achieve controlled, continuous, and prolonged motion. The challenges arise from the typically ill-controlled rate of surfactant release and the quick decay of surface tension gradients due to interfacial surfactant equilibration. While **camphor boats** represent a common example of solid-surfactant-powered Marangoni propulsion and can sustain prolonged motion, they necessitate channels to confine Suematsu et al. (2010) their irregular motion, and speed is not easily adjustable. The subsequent discussion will delve into a more controllable motion.

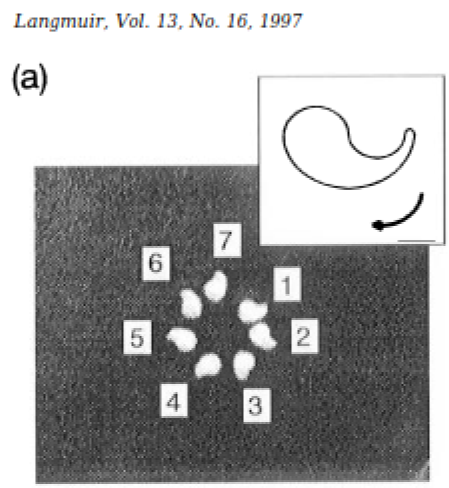

Figure 2.3: Asymmetric Camphor scraphing - inverted comma particle, referenced from Nakata Satoshi & Ose (1997)

2.2.2 Rotational Motion

Rotational and oscillatory motion in camphor particles can be attributed to two distinct mechanics: asymmetry Nakata et al. (2016) or spontaneous symmetry breaking Hayashima et al. (2001). In the first type, motion direction is directly influenced by the asymmetry inherent in the system.

1. Asymmetry in Shape: exhibits unidirectional rotation due to the nonuniform surface tension around the camphor scraping. Unlike translational motion, the direction is dictated by the shape of the camphor scraping. An example of such an achiral shape is the **inverted comma-shaped** camphor particle proposed by Nakata Satoshi & Ose (1997), as depicted in Fig. 2.3. In this configuration, the side of the camphor particle with a smaller outer surface cross-sectional area experiences a larger pull from the liquid, owing to a lower concentration of dissolved camphor particles and higher surface tension at that point. Experimental validation supports the argument, confirming a clockwise rotation.

2. Asymmetry in Surface: Another mechanism involves adjusting the boundary of the chamber Nakata et al. (2016). By manipulating the position of two laterally movable half disks in the experimental model, the symmetry of the boundary is intentionally disrupted, allowing for the attainment of a desired rotational direction, irrespective of the initial rotation state.

3. Spontaneous Symmetry Breaking - Similar to translational motion, this mechanism leads to uncontrollable rotational motion. It occurs when the system's rest state, initially consistent with symmetric properties, becomes unstable, resulting in motion with lower symmetry. For instance, a camphor grain that typically undergoes translational motion was induced to exhibit oscillatory motion Hayashima et al. (2001); Koyano et al. (2017) when placed along the water route.

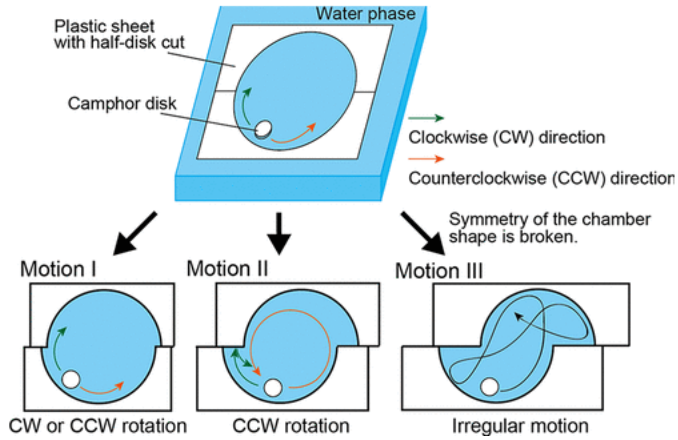

Figure 2.4: Rotation motion due to Asymmetry in boundry surface, referenced from Nakata et al. (2016)

Symmetric camphor particles remain motionless since the dissolved camphor layer around them is uniform. However, irregularities in concentration on the surface can lead to spontaneous symmetry breaking and induce motion. This phenomenon is exemplified in rectangular **camphor ribbons,** created by inducing camphor to paper strips. The irregularities in concentration on the surface cause a breaking of symmetry, making this system rotate when pivoted.

2.2.3 Intermittent Motion

Intermittent motion is closely tied to the translation model of the camphor disk attached to the plastic boat described earlier. In this model, camphor particles diffuse on both sides of the disk at different rates due to varying exposure to the water surface. Experimental observations by Suematsu et al. (2010) revealed that, owing to spontaneous disintegration, the boats decelerate and eventually come to a halt. During the halting period, there is a buildup of diffused camphor particles from below, which subsequently reinitiates the motion. Thus, the system undergoes a continuous cycle of translation-halt-reinitiate, creating intermittent motion.

Having covered the fundamental motions of camphor particles, let's explore how these motions influence one another. The introduction of multiple ribbons adds a layer of complexity as the ribbons interact and couple with each other. This interaction may lead to coordinated or synchronized motions. Understanding how these ribbons interact forms the foundational basis for studying coupled camphor ribbons

2.3 Coupling between camphors

In scenarios involving two or more particles, the camphor layer of each particle on the common water surface serves as a medium for coupling. To verify the coupling of particles in the system, we observe different rhythmic patterns and behaviors, particularly synchronization among them. Various experiments have extensively demonstrated that such systems of rotor particles exhibit synchronization:

1. Translational motion of camphor boats confined in a polygonal chambers (dual circular channel, triangular, cubical channel). - Nakata et al. (2005, 2000)

2. Intermittent motion of collective camphor particles Suematsu et al. (2015) switching between rapid motion and rest.

3. Rotation motion of two pivoted **camphor ribbons. -** Jain et al. (2022, 2023); Sharma et al. (2019)

Among these, synchronization due to intermittent and rotational motion is an emerging field of study as their mechanisms are not fully understood. For intermittent motion, experimental setups demonstrated that the collective motion of particles was not controllable, leading to collision and desynchronization Suematsu et al. (2015). For rotational motion, no mathematical model has been devised to explain spontaneous symmetry breaking Hayashima et al. (2001). Wrapping up this chapter, we introduce the experiment and its modeled potential, which we are about to analyze for stability.

2.3.1 Camphor Ribbons as Coupled Rotors

A camphor ribbon, comprised of a rectangular piece of paper infused with camphor Jain et al. (2022); Sharma et al. (2019) have demonstrated rotational motion when pivoted around a point and placed on the water's surface. This rotational motion arises from the symmetry breaking induced by irregularities in camphor concentration. When two such ribbons are pivoted on a common surface Fig. 2.5, they interact through the dispersed camphor layers around them, resulting in chemical coupling between them. This chemical coupling Sharma et al. (2019) further leads to the synchronization of camphor particles, achieved through either co- or counter-rotation of the ribbons.

2.3.2 Potential of Coupled Rotors

The motion of a single rotor is primarily driven by the concentration gradient of dispersed camphor molecules, causing a decrease in surface tension on one side compared to the other. Consequently, the rotor is pulled toward the side with higher surface tension. From this conceptual framework,

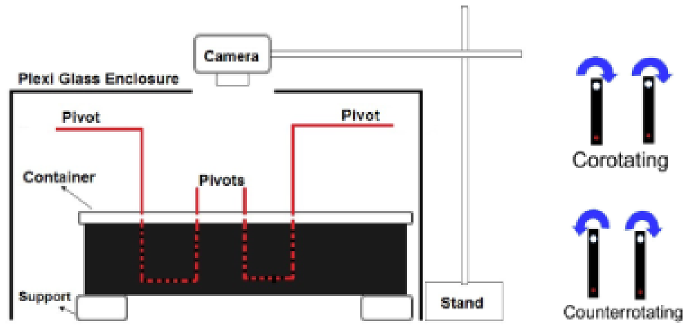

FIG. 1. The schematic side view of the experimental setup (left) and the upper view of the camphor ribbons (right). The white (upper) dots in the ribbons (right) are used to track the ribbon trajectories, while the red (lower) dots indicate the position of the pivot points.

Figure 2.5: Schematics of Camphor rotors experimental setup referenced from Sharma et al. (2019, 2020); Jain et al. (2023, 2022)

one would expect a **repulsive force** when two such rotors approach each other. However, observations from the experimental video revealed a collective motion of two camphor ribbons exhibiting an **attractive nature** when they are within a certain threshold distance r_0 of each other. This attraction corresponds to the interaction between two camphor ribbons in regions of high concentration of dispersed camphor particles. A similar attractive behavior has been reported recently in the context of camphor particles confined to a circular region, where they are drawn towards the circular boundary due to a high concentration of dispersed particles Cruz et al. (2024). It is important to note that despite experimental support for this attractive camphor interaction, no explanation has yet been provided. Previously, this aspect was overlooked, leading to a discrepancy between the observed behavior and the model analysis. Addressing this issue serves as the **primary objective** of this semester's study, which involves devising a new potential that incorporates this attractive nature within a specified threshold distance between the rotors.

It is worth mentioning that previous studies Jain et al. (2022) have examined whether these rotors change direction after collision and have reported that they behave independently when the distance between them is larger, confirming that they are weakly coupled. Mathematically, this weak coupling between two rotors, assuming them to be point particles attached to a pivot, has been previously modeled as a Yukawa-type potential Jain et al. (2022, 2023); Kaiser et al. (2013)

$$\frac{e^{-Kr}}{r}, \tag{2.1}$$

K is coupling parameter determining range of the force

$r(\theta_1, \theta_2)$ is magnitude of relative distance between two router ends, and depends on angle of

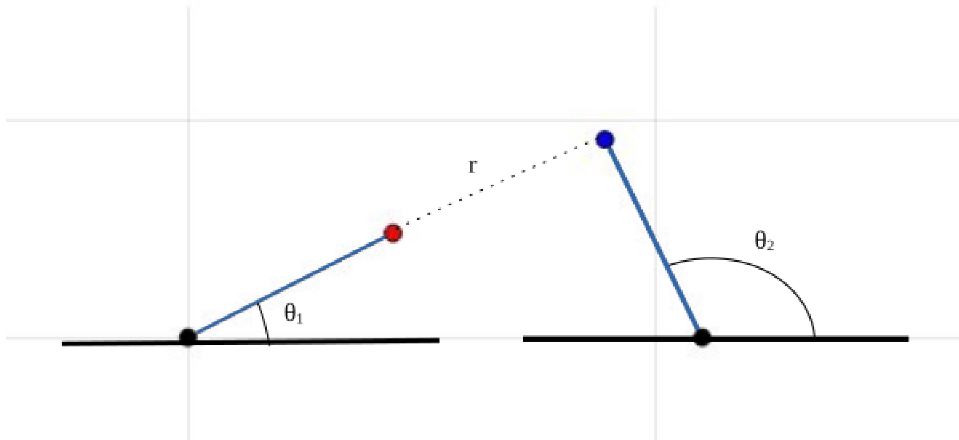

Figure 2.6: System of coupled rotors under point particle approx, black dots are pivots.

rotor arms both being measured counter clockwise, this is depicted in Fig. 2.6

The assumption that rotor ribbons behave as discrete rods, with ends behaving like point particles, is driven by the irregular concentration of camphor at the edges of the paper. This concentration gradient significantly contributes to symmetry breaking, particularly in contrast to the lateral surfaces in contact.

In the upcoming sections, we will highlight the shortcomings of this potential and propose alternative one. Subsequently, we will introduce a potential of the form

$$\frac{1-e^{-Kr^n}}{r} \tag{2.2}$$

with $n > 2$, along with analytical techniques previously introduced to analyze stability. We will then proceed with finding the nature of fixed points and types of synchronization dynamics exhibited between rotors.

Chapter 3

Results & Discussion

3.1 Prelude

Before delving into the study of the newly modeled potential, it is essential to revisit the system outlined in the preceding semester. The experimental setup and the nature of interaction between camphor ribbons were discussed in the last two sections. The upcoming section addresses the limitations identified in the previous modeling approach and outlines the steps taken to address them.

3.1.1 Modeling

In the experimental setup involving interacting camphor ribbons, two fixed points were observed, prompting an investigation into their stability. Initially, we adopted an interaction potential proposed by previous researchers, modeled as $\frac{e^{-Kr}}{r}$. However, stability analysis was hindered as the Jacobian vanished at non-trivial fixed points. To overcome this issue, we introduced an additive parameter, denoted by ξ, to compute the Jacobian at these points. Nonetheless, analysis conducted in the semester III - 2023 revealed instability at these fixed points, contradicting observations from the experimental video. In response, we introduced an additional parameter, α, representing one of the rotor's arm lengths. Despite these adjustments, the system's behavior remained unchanged, prompting us to explore alternative potential forms.

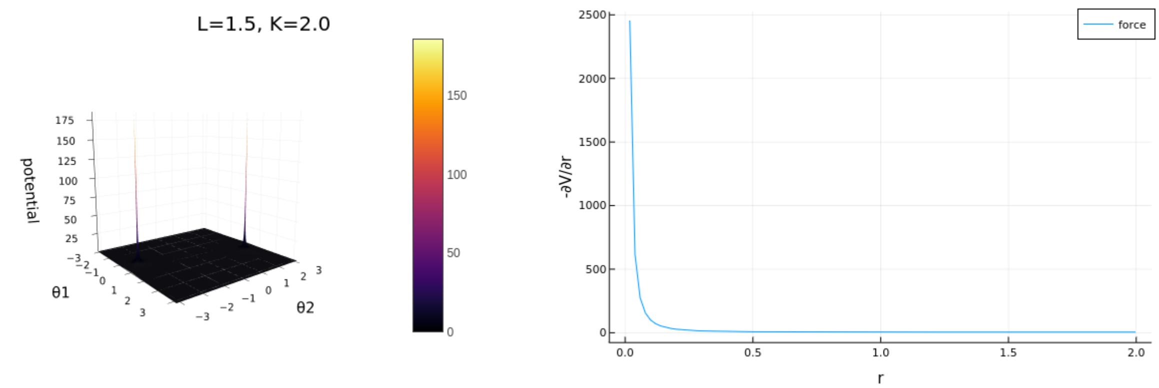

(a) Plot of $V(r)$ vs angle of two rotors (θ_1, θ_2). (b) Plot of force $-\frac{\partial V(r)}{\partial r}$ vs distance r between rotors.

Figure 3.1: Yukawa-type repulsive interaction, $\frac{e^{-Kr}}{r}$.

The plot of the potential in Fig. 3.1a reveals distinct peaks, while Fig. 3.1b confirms the consistently repulsive nature of the force, particularly evident at small distances r. These findings align with our observations of the unstable nature of the fixed points. In the current semester, the focus shifted towards modeling a potential that alternates between repulsive and attractive behavior, with potential minima at the fixed points to reflect their stability.

A promising candidate for this potential was a combination of Coulomb-Yukawa type potentials, expressed as:

$$V(r) = \frac{1 - e^{-Kr}}{r}. \tag{3.1}$$

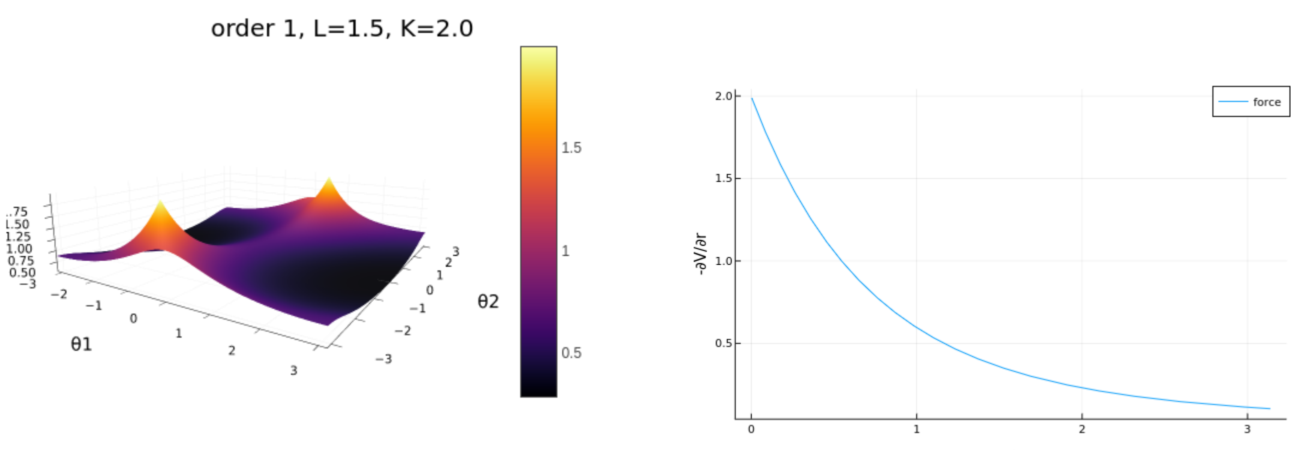

(a) Plot of $V(r)$ vs angle of two rotors (θ_1, θ_2). (b) Plot of force $-\frac{\partial V(r)}{\partial r}$ vs distance r between rotors.

Figure 3.2: Coloumb Yuka-type repulsive interaction, $\frac{1-e^{-Kr}}{r}$

Plotting the potential (see Fig. 3.2) which still exhibits peaks, and confirming the repulsive nature of the force, we decided to explore an exponential function with r^2 in the exponent.

$$V_0(r) = \frac{1-e^{-Kr^2}}{r}. \tag{3.2}$$

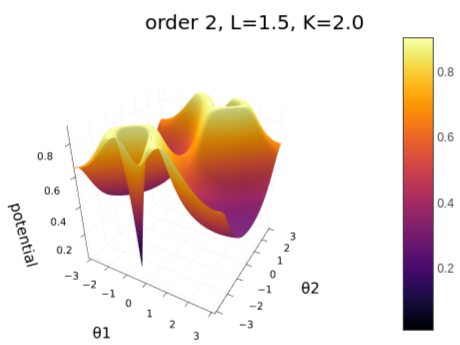

(a) Plot of $V(r)$ vs angle of two rotors (θ_1, θ_2).

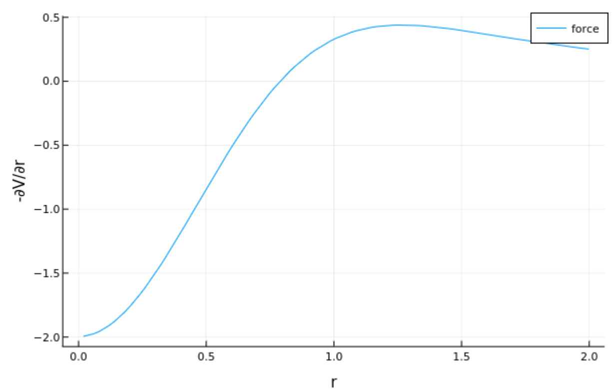

(b) Plot of force $-\frac{\partial V(r)}{\partial r}$ vs distance r between rotors; showing repulsive nature for $r \gtrsim 0.7$.

Figure 3.3: Coulomb Yukawa-type repulsive interaction order 2, $V_0(r) = \frac{1-e^{-Kr^2}}{r}$.

While Fig. 3.3 accurately portrays the desired nature of the potential but the matrix elements of Jacobian diverges to ∞ (see Sec. 3.5) at certain fixed points. Therefore, adopting the same potential form but with $n > 2$ allows us to capture the system's nature and facilitates fixed point analysis.

The potential is represented as:

$$V_0 = \frac{1-e^{-Kr^n}}{r}. \tag{3.3}$$

The remaining analysis is conducted using $n = 3$. Below are the plots (see Fig. 3.4) depicting the potential:

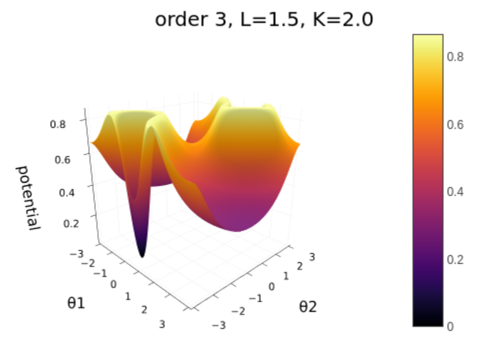

(a) Plot of $V(r)$ vs angle of two rotors (θ_1, θ_2).

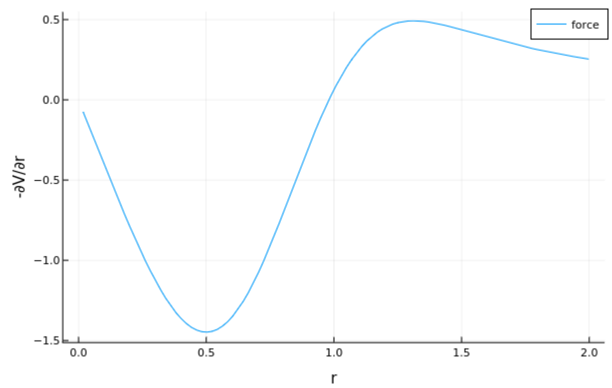

(b) Plot of force $-\frac{\partial V(r)}{\partial r}$ vs distance r between rotors showing repulsive nature for $r \gtrsim 1.0$.

Figure 3.4: Coloumb Yuka-type repulsive interaction $V_0(r) = \frac{1-e^{-Kr^3}}{r}$.

It's worth noting that while we fix $n = 3$ in the upcoming sections, apart from numerical calculations, all analytical frameworks can be encompassed within a common set of system behaviors and features for potentials of the form described by Eq. (3.3) for $n > 2$. Now, we shift our focus to the mathematical calculation of fixed points, time series analysis, Jacobian, and synchronization dynamics.

3.2 Form of central potential

To study dynamical system, we first establish the central potential as

$$V_0 = \frac{1 - e^{-Kr^3}}{r} \tag{3.4}$$

and identify the key parameters that define the system's behavior. These parameters include

L, representing the distance between the two pivots of the rotors, as illustrated in Fig. (3.5).

K, dictates the exponential factor determining the strength of coupling

α, accounts for normalized length of the rotor's arm.

With these parameters established, we embark on an exploration of the coupled rotor dynamics, focusing initially on an analysis where K and α are fixed at 2.0 and 1.0, respectively, while L is varied to investigate its impact on the system. This investigation aims to uncover how changes in L influence the stability and dynamics of the coupled rotors.

Subsequent sections delve into the analytical framework of the system, starting with the derivation of a differential equation from the Hamiltonian. The focus remains primarily on one particular case for identifying fixed points, reserving the exploration of the second case for future analysis. These fixed points are then categorized as trivial or non-trivial, followed by the determination of their eigenvalues via the Jacobian matrix. Numerical results are subsequently presented to validate the analytical findings.

Furthermore, additional tools are introduced to gain further insights into the system's behavior before concluding with a dedicated section on synchronization.

3.3 Governing Equations

We reiterate the parameters L, K, and α and introduce the vector $\vec{r}$, which represents the distance between the end points of the rotor in Fig. 3.5.

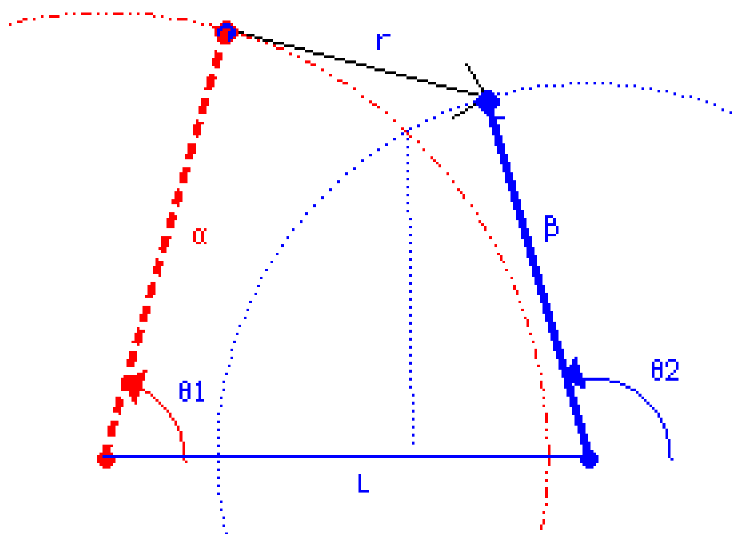

Figure 3.5: Modeled potential for varied length of rotor arms.

Using trigonometry, the following relation for $r(\theta_1, \theta_2)$ can be found:

$$\begin{aligned}\vec{r}(\theta_1,\theta_2) =& (\alpha\cos\theta_1 - \beta\cos\theta_2 - L, \alpha\sin\theta_1 - \beta\sin\theta_2)\\ =& \beta(\frac{\alpha}{\beta}\cos\theta_1 - \cos\theta_2 - \frac{L}{\beta}, \frac{\alpha}{\beta}\sin\theta_1 - \sin\theta_2).\end{aligned}$$

Since β is factored out of r, $\frac{1}{\beta}$ can be absorbed into α and L. Now analysis can be proceeded in terms of the normalized single parameter α. The vector $\overrightarrow{r}(\theta_1,\theta_2)$ becomes

$$\begin{aligned}
\overrightarrow{r}(\theta_1,\theta_2) =& (\alpha\cos\theta_1 - \cos\theta_2 - L, \alpha\sin\theta_1 - \sin\theta_2).\\
|\vec{r}|^2 =& \alpha^2\cos^2\theta_1 + \cos^2\theta_2 + L^2 - 2\alpha\cos\theta_1\cos\theta_2\\
&+ 2\cos\theta_2 L - 2\alpha\cos\theta_1 L + \alpha^2\sin^2\theta_1 + \sin^2\theta_2 - 2\alpha\sin\theta_1\sin\theta_2 \qquad (3.5)\\
r =& \sqrt{\alpha^2 + 1 + L^2 - 2L(\alpha\cos\theta_1 - \cos\theta_2) - 2\alpha\cos(\theta_1-\theta_2)}. \qquad (3.6)
\end{aligned}$$

Computing the derivative of $\theta_1$with respect to r crucial for subsequent analysis, yields

$$\begin{aligned}
2r\frac{\partial r}{\partial\theta_1} &= 2\alpha L\sin\theta_1 + 2\alpha\sin(\theta_1-\theta_2)\\
\frac{\partial r}{\partial\theta_1} &= \alpha(L\sin\theta_1 + \sin(\theta_1-\theta_2))\frac{1}{r}, \qquad (3.7)
\end{aligned}$$

and similarly for θ_2,

$$\begin{aligned}
2r\frac{\partial r}{\partial\theta_2} &= -2\alpha L\sin\theta_2 - 2\alpha\sin(\theta_1-\theta_2)\\
\frac{\partial r}{\partial\theta_2} &= (-L\sin\theta_2 + \alpha\sin(\theta_2-\theta_1))\frac{1}{r}. \qquad (3.8)
\end{aligned}$$

The Lagrangian of a system is given by $\mathscr{L} = T - V$, the potential was proposed without considering the diffusion effect, so mass of the ribbon ends are normalized. Hence, it takes up the form

$$\mathscr{L} = \frac{1}{2}((\alpha\dot{\theta}_1)^2 + \dot{\theta_2}^2) - V_0(r), \qquad (3.9)$$

conjugate momenta are found by

$$p_1 = \frac{\partial\mathscr{L}}{\partial\theta_1} = \alpha^2\dot{\theta}_1 \qquad (3.10)$$

$$p_2 = \frac{\partial\mathscr{L}}{\partial\theta_2} = \dot{\theta}_2. \qquad (3.11)$$

Hence, Hamiltonian for the above system is given by,

$$\begin{aligned}
\mathscr{H} &= \sum p_i\dot{\theta}_i - \mathscr{L}\\
&= (\alpha^2\dot{\theta}_1)\dot{\theta}_1 + (\dot{\theta}_2)\dot{\theta}_2 - \mathscr{L}\\
\mathscr{H} &= \frac{1}{2}((\alpha\dot{\theta}_1)^2 + \dot{\theta_2}^2) + V_0
\end{aligned}$$

using Eq. (3.10,3.11) $\mathscr{H}$ becomes,

$$\mathscr{H} = \frac{1}{2}\big((\frac{p_1}{\alpha})^2 + p_2^2\big) + V_0. \tag{3.12}$$

Equations of motions are

$$\begin{aligned}
\dot{\theta}_1 &= \frac{\partial \mathscr{H}}{\partial p_1} \\
&= \frac{p_1}{\alpha^2} \\
-\dot{p}_1 &= \frac{\partial \mathscr{H}}{\partial \theta_1} \\
&= \frac{\partial V_0}{\partial \theta_1} = \frac{\partial V_0}{\partial r}\frac{\partial r}{\partial \theta_1}.
\end{aligned}$$

Following similar simplification, we derive the differential equations governing the system's motion as:

$$\dot{\theta}_1 = \frac{p_1}{\alpha^2} \tag{3.13}$$

$$\dot{p}_1 = -\frac{\partial V_0}{\partial r}\frac{\partial r}{\partial \theta_1} \tag{3.14}$$

$$\dot{\theta}_2 = p_2 \tag{3.15}$$

$$\dot{p}_2 = -\frac{\partial V_0}{\partial r}\frac{\partial r}{\partial \theta_2}. \tag{3.16}$$

3.4 Fixed points

To conduct fixed point analysis, we aim to find points where all time derivatives simultaneously vanish. This allows us to determine the long time behaviour of the system. Since we now have the differential equations describing the system's behavior, Eq. (3.13-3.16) are zero at these fixed points. This occurs when the following conditions are met simultaneously:

$$\dot{\theta}_1 = p_1 = 0 \tag{3.17}$$

$$\dot{\theta}_2 = p_2 = 0, \tag{3.18}$$

combining Eq (3.14, 3.16):

$$\dot{p}_j = -\frac{\partial r}{\partial \theta_j}\frac{\partial V_0}{\partial r} = 0. \tag{3.19}$$

Below are the two cases where these condition are satisfied:

Case I $\frac{\partial r}{\partial \theta_j} = 0$.

$\frac{\partial r}{\partial \theta_j}$ have been computed before Eq. (3.7), (3.8) and for the fixed points these are equated to 0

$$0 = \alpha(L\sin\theta_1 + \sin(\theta_1 - \theta_2)) \tag{3.20}$$

$$0 = -L\sin\theta_2 + \alpha\sin(\theta_2 - \theta_1), \tag{3.21}$$

adding equations Eq. (3.20) and Eq. (3.21) we arrive at

$$\alpha\sin\theta_1 = \sin\theta_2. \tag{3.22}$$

Eqs. (3.20-3.22) combined give rise to set of 9 trivial fixed points which can be grouped into 3 based on the following arguments: Since, we are measuring the angle in the counterclockwise sense, the points $(\pi,0,0,0)$, $(-\pi,0,0,0)$ are the same, similarly, $(0,0,\pm\pi,0)$ are also same. In Fig. 3.6a 1^{st} and 4^{th} configurations are mirror configurations . Concluding, there are only 3 unique configurations $(S1,S2,S3)$ corresponding to the 9 fixed points.

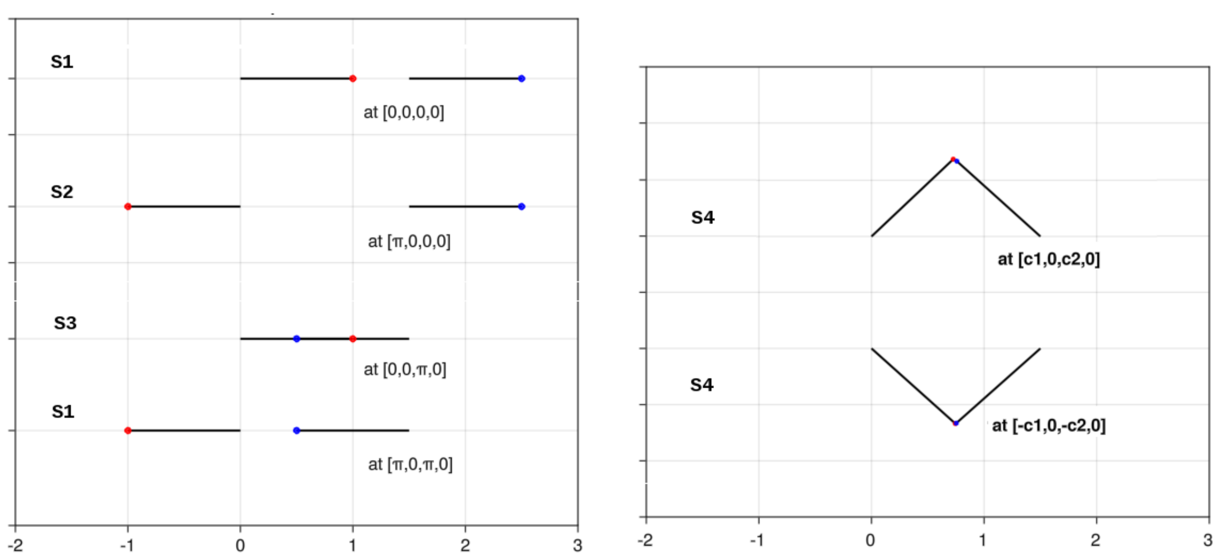

(a) Trivial fixed points.

(b) Non trivial fixed points - collision points.

Figure 3.6: Configurations corresponding to fixed points, one of the ribbon is pivoted at $(0,0)$ (red dot at its end), other at $(1.5,0)$.

Also, Eq. (3.20) and Eq. (3.21) are transcendental equations and plot for different values of L in Fig. 3.7 depicts another set of solutions (S4 - see Fig. 3.6b), when $L < 1+\alpha$ and $L > |1-\alpha|$. The former condition corresponds to case of collision while the later represents the scenario when smaller circle resides inside the bigger. The collision points[1] take up the form of

$$(c_1, c_2), (-c_1, -c_2) \tag{3.23}$$

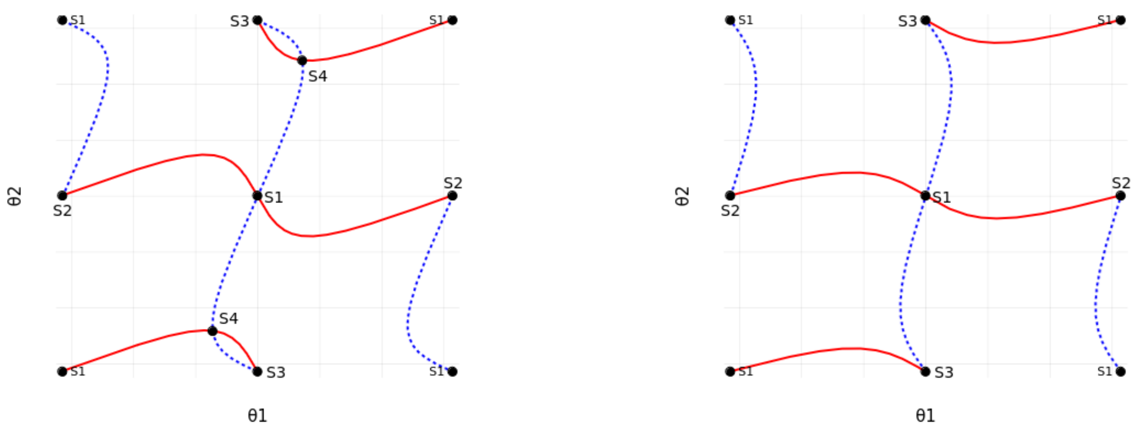

(a) for $L = 1.5$.

(b) for $L = 2.5$.

Figure 3.7: Plot of Eq. (3.20)-dotted, Eq. (3.21) showing (c_1, c_2) vanishes after $L = 2.0$.

System configuration - $(S4)$ for these points are shown in Fig. 3.6b. The plot (see Fig. 3.7b) as well as bifurcation plot - Fig. 3.8 depicts the condition for existence of these points.

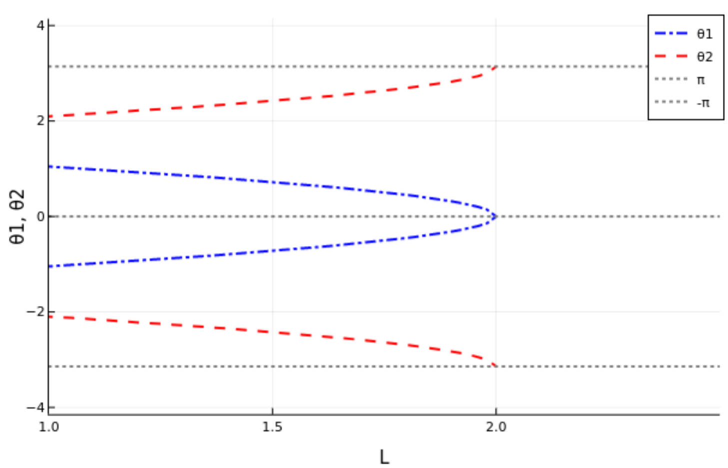

Figure 3.8: The bifurcation plot depicted in Fig. 3.6b illustrates collision points corresponding to system configuration $(S4)$. Curves on the positive (θ_1, θ_2) axis represent (c_1, c_2) at specific values of L, while those on the negative axis represent $(-c_1, -c_2)$. It becomes evident that after $L = 2.0$, these points converge to the trivial fixed points of configuration $(S3)$, i.e., $(c_1, c_2) \to (0, \pi)$ and $(-c_1, -c_2) \to (0, -\pi)$.

[1] For $L = 1.5$, $(c_1, c_2) \approx (0.7, 2.4)$

Case II $\frac{\partial V_0}{\partial r} = 0$.

Eq. (3.21) also vanishes when first factor is 0,

$$\frac{\partial V_0}{\partial r} = -(e^{Kr^3} - 3Kr^3 - 1)\frac{e^{-Kr^3}}{r^2} \tag{3.24}$$

$$0 = e^{Kr^3} - 3Kr^3 - 1. \tag{3.25}$$

Plot of above along with Case I conditions are depicted in Fig. 3.9,

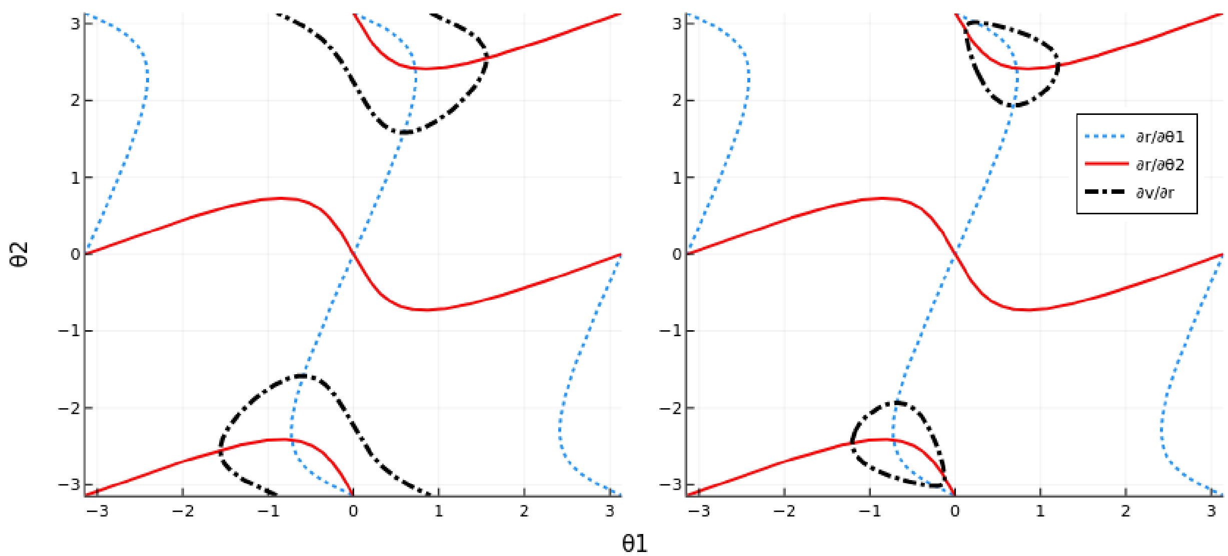

Figure 3.9: For $L = 1.5$ and $K = 2.0, 5.5$; as the value of K increases, Eq. (3.25-black dash dotted) converges to (c_1, c_2).

An initial examination suggests that at large values of K, Case II transitions to Case I. However, we are deferring further exploration of this transition for the time being. Moving forward, in the next section we compute the Jacobian matrix for the fixed points identified from Case I to assess their stability.

3.5 Stability Analysis

The study of fixed points in nonlinear systems involves linearization around fixed points (see Sec. 1.4.1) and determining the eigenvalues/eigenvectors of the Jacobian. This process is applicable to the equations Eq (3.13-3.16) and using the condition $\frac{\partial r}{\partial \theta_j} = 0$ (case I), $\mathscr{J}$ can be simplified as

$$
\mathscr{J} = \begin{bmatrix} 0 & \frac{1}{\alpha^2} & 0 & 0 \\ -\frac{\partial V_0}{\partial r}\frac{\partial^2 r}{\partial \theta_1^2} & 0 & -\frac{\partial V_0}{\partial r}\frac{\partial^2 r}{\partial \theta_1 \partial \theta_2} & 0 \\ 0 & 0 & 0 & 1 \\ -\frac{\partial V_0}{\partial r}\frac{\partial^2 r}{\partial \theta_1 \partial \theta_2} & 0 & -\frac{\partial V_0}{\partial r}\frac{\partial^2 r}{\partial \theta_2^2} & 0 \end{bmatrix}. \tag{3.26}
$$

Factors required for computation of above matrix elements are Eq. (3.24) and following,

$$
\frac{\partial^2 r}{\partial \theta_1^2} = \alpha(Lcos(\theta_1) + cos(\theta_1 - \theta_2))\frac{1}{r} \tag{3.27}
$$

$$
\frac{\partial^2 r}{\partial \theta_2^2} = (-Lcos(\theta_2) + \alpha cos(\theta_1 - \theta_2))\frac{1}{r} \tag{3.28}
$$

$$
\frac{\partial^2 r}{\partial \theta_1 \partial \theta_2} = \alpha(-cos(\theta_1 - \theta_2))\frac{1}{r}. \tag{3.29}
$$

Upon substituting the fixed points into the expressions above, our goal is to compute the Jacobian matrix as given in Eq. (3.26). However, we encounter a complication during this process. Specifically for configuration $S4$ i.e. at the non-trivial points (c_1, c_2) and $(-c_1, c_2)$ these expressions become **infinite**. This issue arises due to the presence of the factor $\frac{1}{r}$ in the equation. This underscores the necessity of having $n > 2$ in the modeled potential. Before delving deeper into this issue, we first proceed to analyze the stability of the trivial fixed points.

3.5.1 Trivial Fixed Points

We identified three unique groupings of trivial fixed points $(S1, S2, S3)$ from Fig. 3.6a. Now, we proceed to visualize the behavior of the system by plotting the maximum of real eigenvalues against parameters L (see Fig. 3.10) . To further validate the analytical result, we employ numerical techniques to integrate ODEs, specifically Runge-Kutta methods (RK4) with a time step of 0.0001. Subsequently, we plot time series data for θ_1 and θ_2.

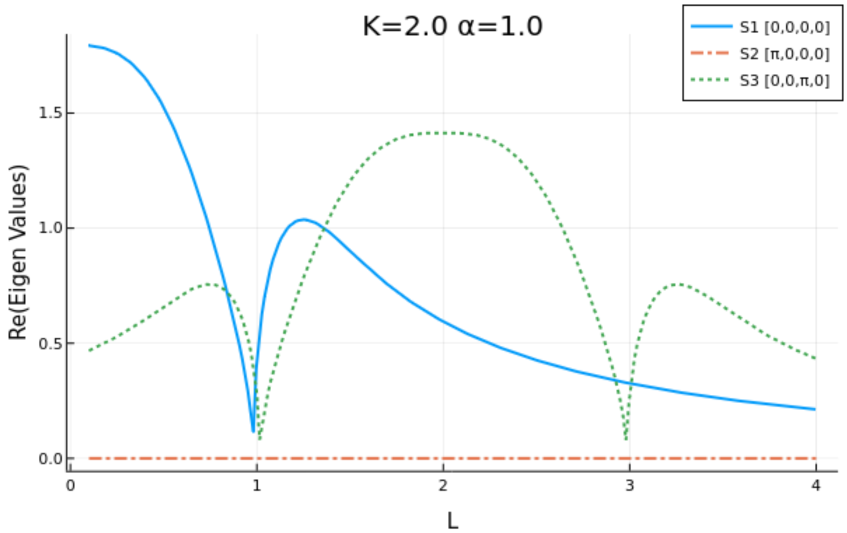

Figure 3.10: Variation of eigenvalues of 3 trivial configurations $(S1, S2, S3)$ Fig. (3.6a) vs length between rotors.

- $S1$ - $(0,0,0,0)$,$(\pm\pi,0,\pi,0)$,$(\pm\pi,0,-\pi,0)$ - Eigenvalues for the fixed points exhibit both real and complex components. The plot (see Fig. (3.10) consistently displays a positive real part, leading to the classification of these points as **saddle points**, as indicated. This is also backed by the numerical integration carried near $S1$, spanning $[-1,1]$ in Fig. 3.11.

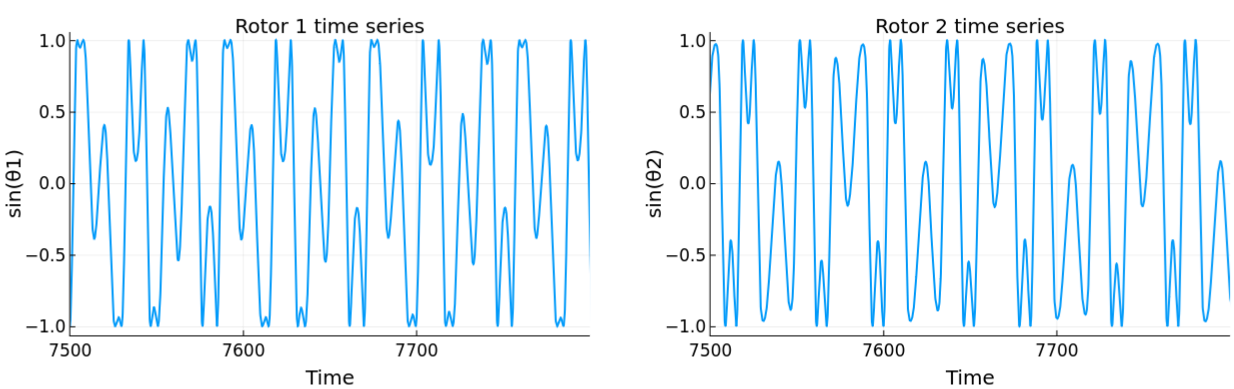

Figure 3.11: Time series of rotors started near $(0,0,0,0)$

- $S2$ - $(\pm\pi,0,0,0)$ - Plot of eigenvalues for different values of L in Fig. 3.10 show there's no real part, Hence eigen-values are purely imaginary and these are classified as **centre** i.e., perturbing little from the point will undergo oscillatory motion, this is evident from time series plot in Fig. 3.12.

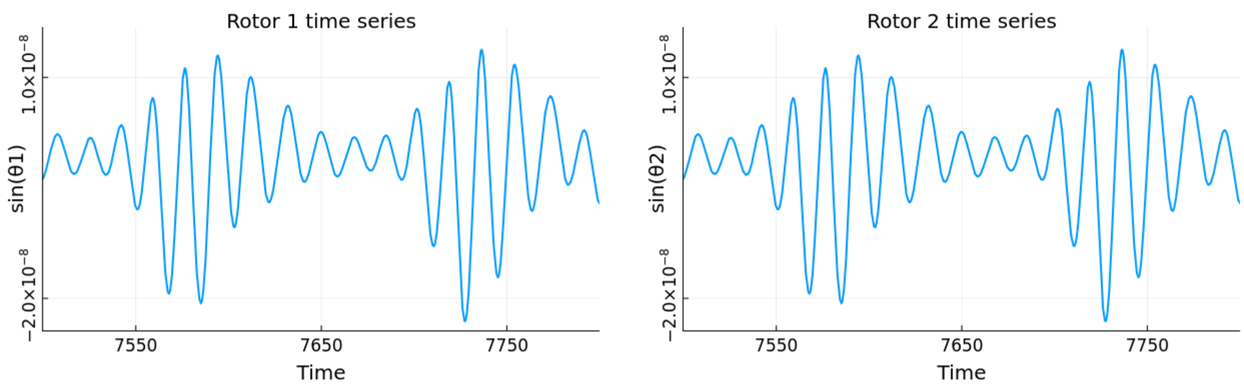

Figure 3.12: Time series of rotors started near $(\pm\pi, 0, 0, 0)$. Span of $\sin(\theta_1)$ and $\sin(\theta_2)$ are symmetric and very small indicating behaviour of centre.

- $S3$ - $(0, 0, \pm\pi, 0)$ - This point resembles the configuration at $(0, 0, 0, 0)$ exhibiting **saddle** behavior. The plot of eigenvalues reveals a significant divergence at $L = 2$, Fig. 3.10. Also numerical analysis backups up this observation (see Fig. 3.13).

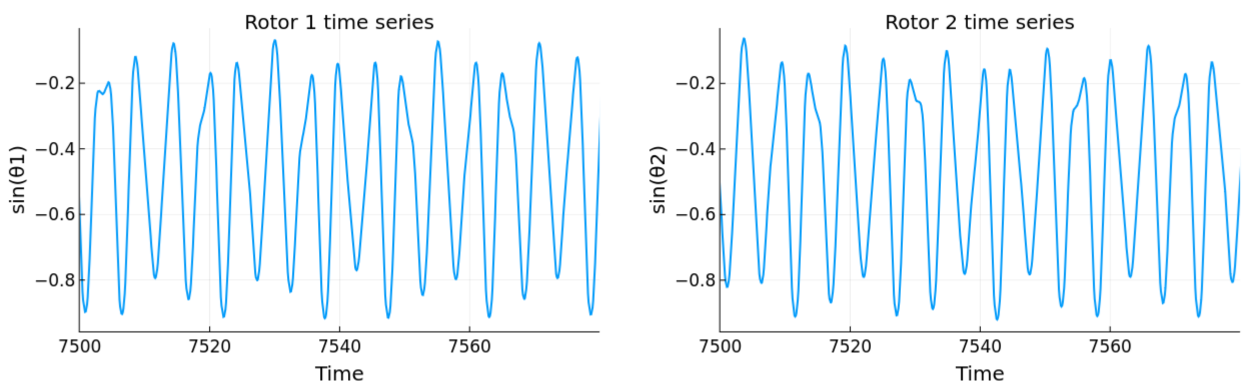

Figure 3.13: Time series of rotors started near $(0, 0, \pm\pi, 0)$.

3.5.2 Non Trivial Fixed Points

It is known that at collision points, $r \to 0$[2] corresponding to $(S4)$ configuration in Fig. 3.6b and matrix elements of $\mathscr{J}$ tends to ∞ due to presence of $\frac{1}{r}$, this was briefly addressed at end of Sec. 3.5. To overcome this issue, we use Taylor expansion for the potential around $r = 0$,

$$V_0 = \frac{1 - e^{-Kr^3}}{r} = \frac{1}{r} - \frac{1}{r} + Kr^2 - \frac{1}{2}K^2r^5 + .. \tag{3.30}$$

$$V_0 \approx Kr^2 - \frac{1}{2}K^2r^5. \tag{3.31}$$

[2] distance between ends of two rotors

Higher order terms removal was justified at $r = 0$ (see Fig. 3.14). Now taking derivative of above with respect to r, we get

$$\frac{\partial V_0}{\partial r} = 2Kr(1 - \frac{5}{4}kr^3). \tag{3.32}$$

Upon comparing this with the non-truncated potential given by Eq. (3.24), it becomes apparent that the latter has a factor of r^2 in the denominator, while the former equation's r in the numerator cancels out with Eqs. (3.27-3.29), thus removing the singularity. Consequently, the Jacobian was calculated using Eq. (3.31) at the point (c_1, c_2). The resulting eigenvalues are purely imaginary $(\pm 2.120i, \pm 1.870i, \pm 2.120i, \pm 1.870i)$, indicating that the fixed point is a center. This observation is further supported by numerical integration, as illustrated in Fig. 3.15.

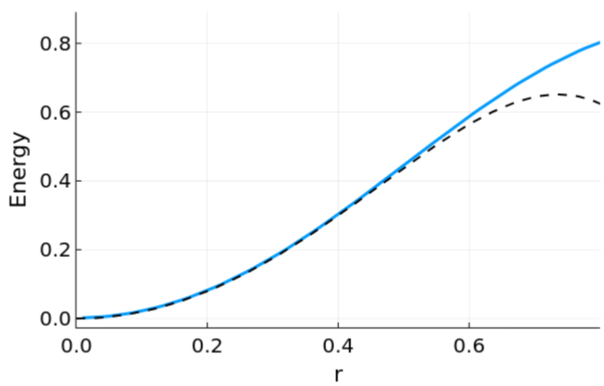

Figure 3.14: Comparison of potential V_0 described by Eq. (3.30) - (solid blue) with its Taylor-expanded approximation truncated at the second order, $V_0 \approx Kr^2 - \frac{1}{2}K^2r^5$ (dashed black) evaluated at $r = 0$.

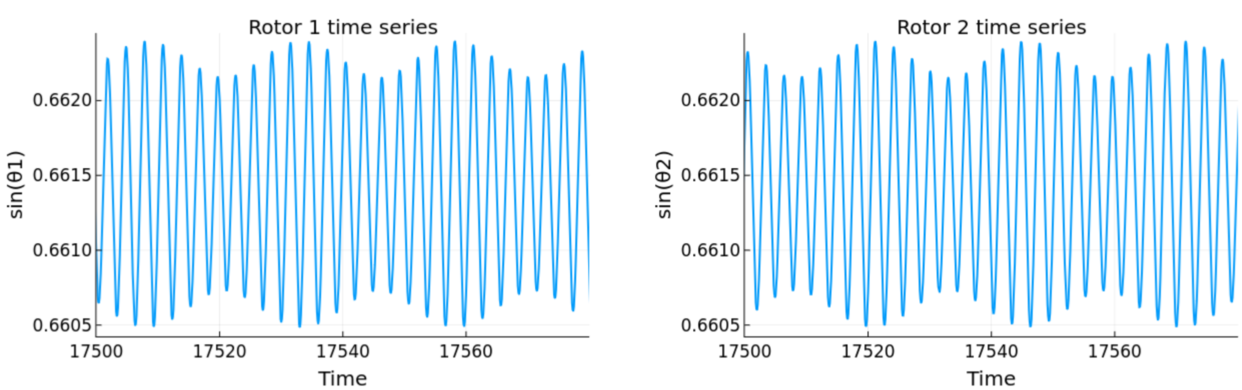

Figure 3.15: Time series of rotors started close to (c_1, c_2).

Up-to this point, our analysis of the new potential has led to successful replication of the experimental video, confirming the classification of the fixed point as a center both numerically and analytically. However, this achievement alone is insufficient. To further validate our results, we compare them with those of the previously studied model by Jain et al. (2023, 2022), which not only provided analytical conditions for synchronization but also demonstrated coherence with experimental data. Through this comparison, we can suggest that our new potential is a valid candidate for replicating the actual dynamical system of coupled rotors. In the upcoming section, we will verify the previously established results.

3.6 Synchronization[3]

In the realm of synchronization, when the two rotors synchronize, we can get insights about the dynamics of one rotor by observing the other. For phase synchronization, this is characterized by a condition expressed as

$$|\theta_1| - |\theta_2| \leq constant, \tag{3.33}$$

where both θ_1 and θ_2 are measured in the anticlockwise direction Fig. (3.33). For coherence, we consider both co- and counter-rotating ribbons, taking the absolute values of the phases θ_1 and θ_2. In counter-rotation synchronization, the angles of the two rotors change in opposite directions over time (one clockwise and the other counterclockwise), while in co-rotation synchronization, both angles vary in the same direction.

Now, by taking the time derivative of Eq. (3.33) and substituting the relations from Eqs. (3.10-3.11), we find $|\frac{p_1}{\alpha}| - |p_2| \sim 0$. However, since our dynamical system is governed by equations such as Eqs. (3.13,3.16), which involve derivatives of these variables, we prefer to utilize them instead. Additionally, we incorporate the modulus operator at the end of the calculation, resulting in the following equations,

$$\begin{aligned} \frac{\dot{p}_1}{\alpha} - \dot{p}_2 &= 0 \\ -\frac{\partial V_0}{\partial r}\frac{\partial r}{\partial \theta_1} + \frac{\partial V_0}{\partial r}\frac{\partial r}{\partial \theta_2} &= 0 \\ -\frac{\partial V_0}{\partial r}\left(\frac{\partial r}{\partial \theta_1} - \frac{\partial r}{\partial \theta_2}\right) &= 0. \end{aligned} \tag{3.34}$$

The mentioned analysis was conducted by setting the second factor from the above to 0. Substituting the relations from Eqs. (3.7,3.8) with $\alpha = 1$, we obtain:

[3]This section is grounded in the synchronization condition reported by Jain et al. (2023) in Section III, Results and Discussion, page 4.

$$
\begin{aligned}
0 &= L\sin\theta_1 + \sin(\theta_1-\theta_2) - (-L\sin\theta_2 \\
&\quad + \sin(\theta_2-\theta_1)) && (3.35)\\
L(\sin\theta_1+\sin\theta_2) &= 2\sin(\theta_2-\theta_1)\\
\sin\theta_1+\sin\theta_2 &= \frac{2}{L}\sin(\theta_2-\theta_1). && (3.36)
\end{aligned}
$$

Due to $|\sin(\theta_2-\theta_1)| \leq 1$, the absolute value of the left-hand side of the above equation is always less than $\frac{2}{L}$. Thus, it becomes:

$$
\begin{aligned}
|\sin\theta_1+\sin\theta_2| &\leq \frac{2}{L}\\
|\sin\theta_1-\sin(-\theta_2)| &\leq \frac{2}{L}\\
||\sin(\theta_1)|-|\sin(-\theta_2)|| &\leq \frac{2}{L}. && (3.37)
\end{aligned}
$$

The above equation was simplified using the triangle inequality $|a-b| \geq ||a|-|b||$. Further simplification yields the condition for synchronization as follows:

$$
\frac{-2}{L} \leq |\sin(\theta_1)|-|\sin(\theta_2)| \leq \frac{2}{L}. \tag{3.38}
$$

Choosing initial conditions[4] such that they undergo quasi-periodic motion, we can then use condition Eq. (3.33) to verify where they are synchronized or not.

Figs. 3.16, 3.17 depicts two such initials conditions for $L = 1.5$ where they undergo counter rotating synchronized out-of-phase oscillations, and Figs. 3.16b, 3.17b validates the established condition with max amplitude of $|\sin(\theta_1)|-|\sin(\theta_2)| < 0.06$ which is well less than the limit established by Eq. (3.38) i.e. $\frac{2}{L} \sim 1.33$.

[4]Simulated videos directory - Google drive

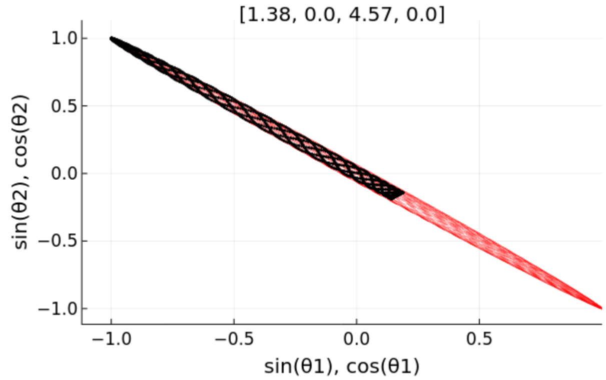

(a) Plot of sine (out-of-phase red) and cosine (out-of-phase black) of the angles between the two rotors.

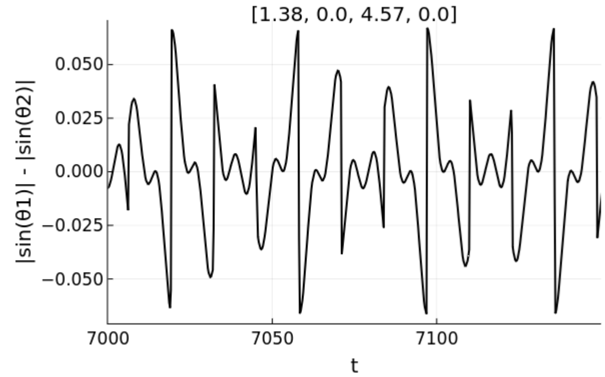

(b) The maximum amplitude of $|\sin(\theta_1)| - |\sin(\theta_2)|$ is less than 0.06, which significantly falls below the synchronization threshold of $\frac{2}{L} \approx 1.33$ established in Eq. (3.38)

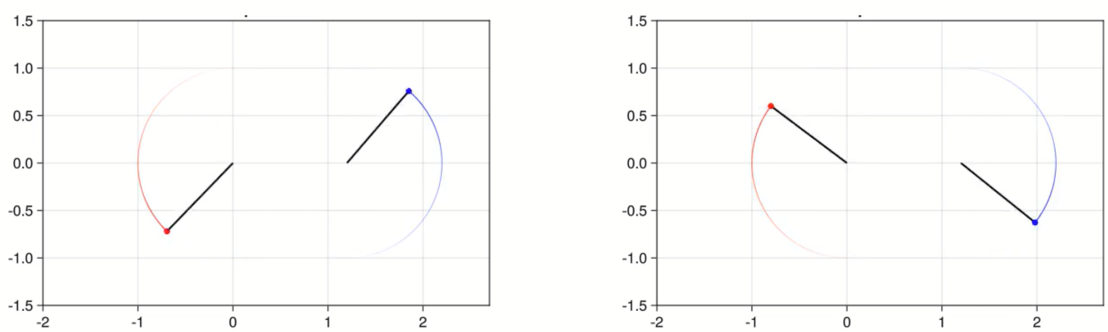

(c) Frames of animation

Figure 3.16: Considering the initial condition $(1.38, 0.0, 4.57, 0.0)$ with parameters $(K, L) = (2.0, 1.5)$, the system was numerically integrated with a step size of 10^{-4}. Plotting sin and cosine of angle between the two rotors, as shown in Fig. 3.16a, we observe synchronized out-of-phase oscillations, which is further supported by visual evidence Fig. 3.16c. The synchronization is also analytically validated using the condition depicted in Fig. 3.16b.

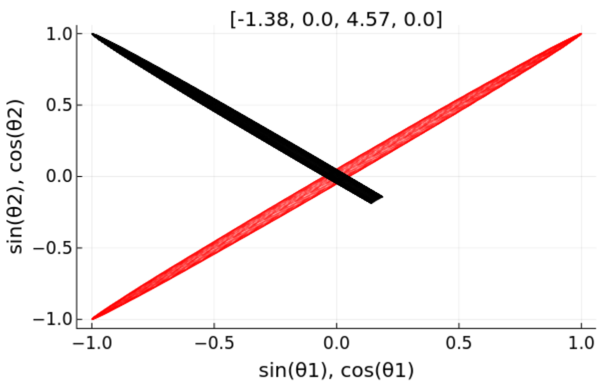

(a) Plot of sine (in-phase red) and cosine (out-of-phase black) of the angles between the two rotors.

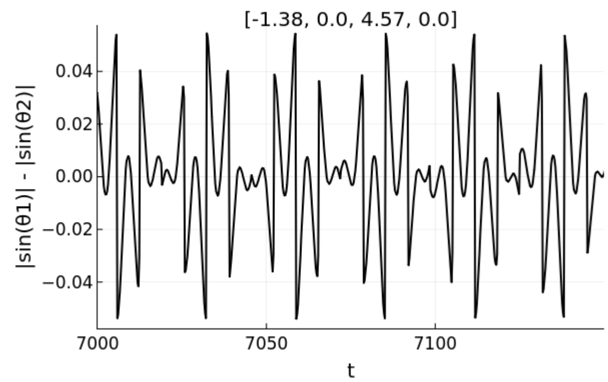

(b) The maximum amplitude of $|\sin(\theta_1)| - |\sin(\theta_2)|$ is less than 0.05, which significantly falls below the synchronization threshold of $\frac{2}{L} \approx 1.33$ established in Eq. (3.38) sync condition

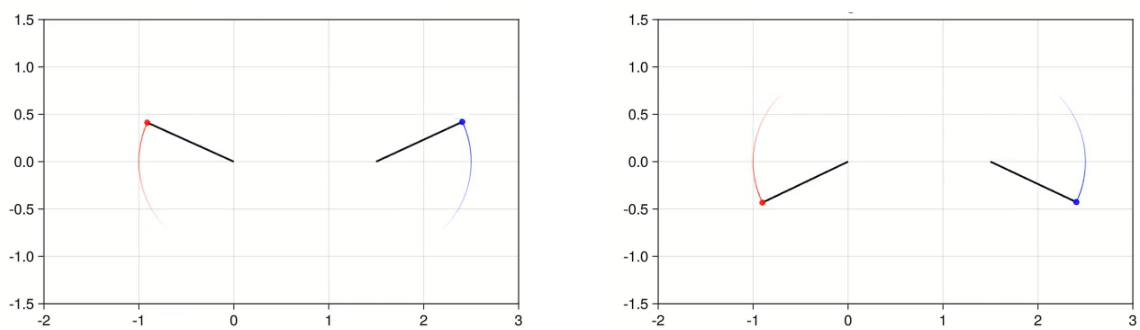

(c) Frames of animation

Figure 3.17: Considering the initial condition $(-1.38, 0.0, 4.57, 0.0)$ with parameters $(K, L) = (2.0, 1.5)$, the system was numerically integrated with a step size of 10^{-4}. Plotting sin and cosine of angle between the two rotors, as shown in Fig. 3.17a, we observe synchronized out-of-phase oscillations, which is further supported by visual evidence Fig. 3.17c. The synchronization is also analytically validated using the condition depicted in Fig. 3.17b.

The experimental data presented in Fig. 3.18 from the previous paper Jain et al. (2023) illustrated the synchronization behavior for different values of L. It demonstrates how synchronization conditions fail for larger distances L, indicating that due to weak coupling rotors behave more independently and result in quasi-periodic motion without synchronization.

To compare our model with the experimental data, as shown in Fig. 3.19, we consider an initial condition $(0.08, 0.8, 0.0, -1.1)$, initially synchronized quasi-periodic motion. We then increase the value of L from 1.5 to 5.0 and observe the desynchronization as the distance between the rotors increases. This observation is consistent with the synchronization condition, both analytically and experimentally.

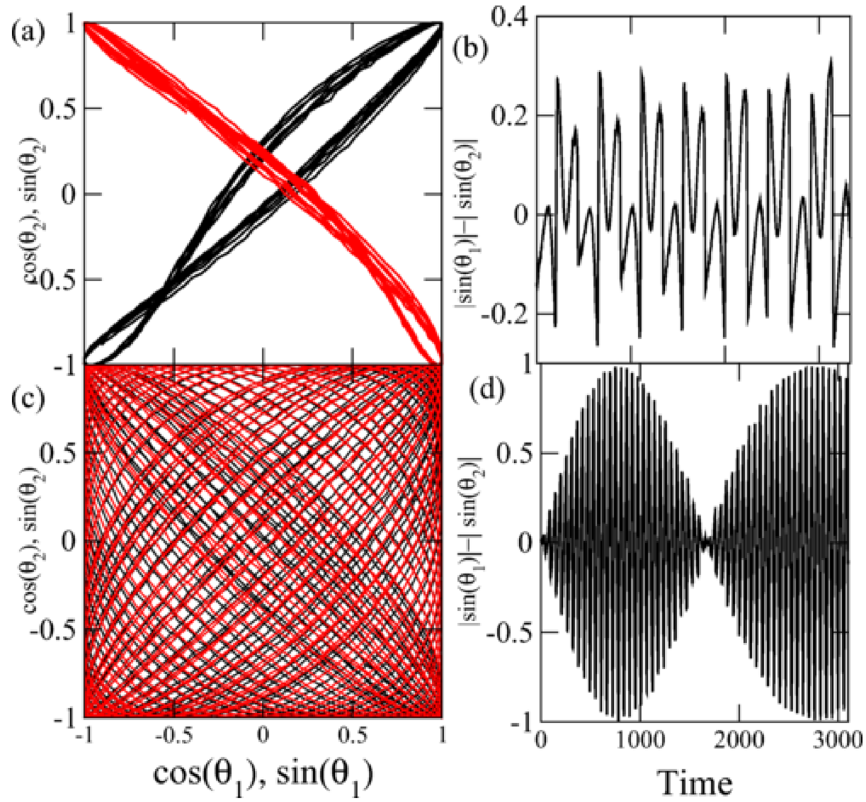

Figure 3.18: In the experimental data reported by Jain et al. (2023), captured at a frame rate of 120 Hz (Page 6), the left column plots show $\sin\theta_1$ vs $\sin\theta_2$ (red) and $\cos\theta_1$ vs $\cos\theta_2$ (black) for different values of L,specifically $3,0$ and 6.0. The top-right figure illustrates a maximum amplitude of $|\sin(\theta_1)| - |\sin(\theta_2)| \approx 0.3$, which is below the synchronization threshold of $\frac{2}{L} = \frac{2}{3} \approx 0.67$, indicating synchronized motion. Conversely, for a greater value of $L = 6.0$, the bottom-right figure shows a maximum amplitude of $|\sin(\theta_1)| - |\sin(\theta_2)| \approx 1$, exceeding the synchronization threshold of $\frac{2}{L} \approx \frac{2}{6} \approx 0.33$, resulting in unsynchronized motion. This disparity is further evident in the sine and cosine plots of the angles on the left.

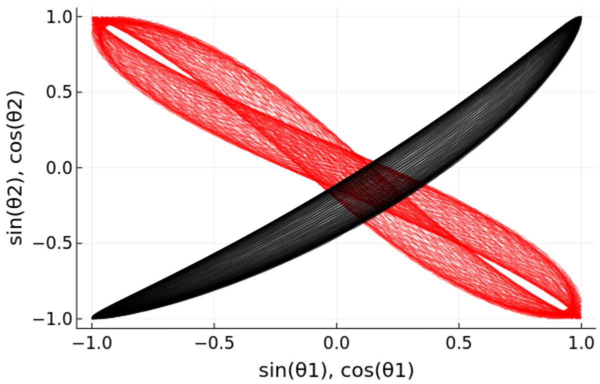

(a) For $L = 1.5$, sine (red) and cosine (black) of angles

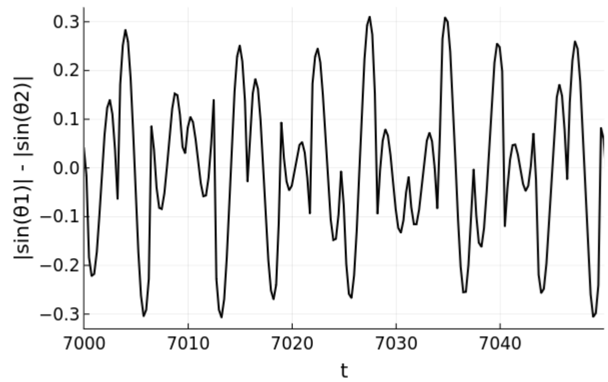

(b) $\max(|\sin(\theta_1)| - |\sin(\theta_2)|) \sim 0.3$, $\frac{2}{L} = \frac{2}{1.5} \approx 1.33$

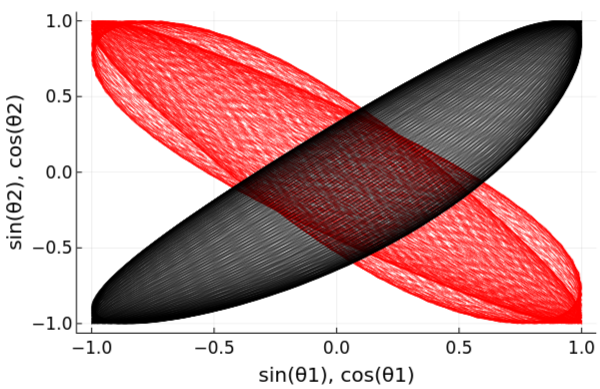

(c) For $L = 3.0$

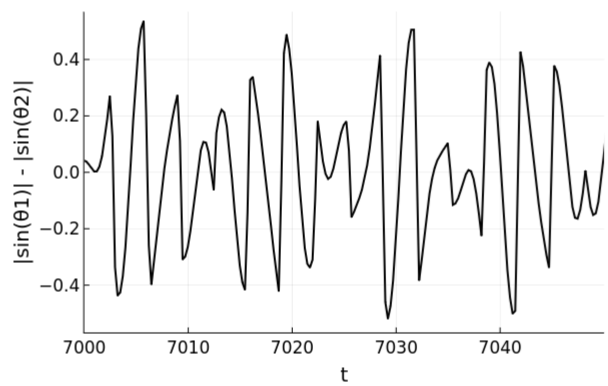

(d) $\max(|\sin(\theta_1)| - |\sin(\theta_2)|) \sim 0.5$, $\frac{2}{L} = \frac{2}{3.0} \approx 0.67$,

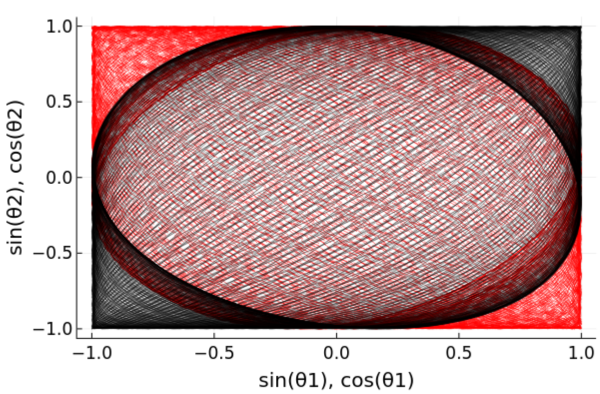

(e) For $L = 5.0$

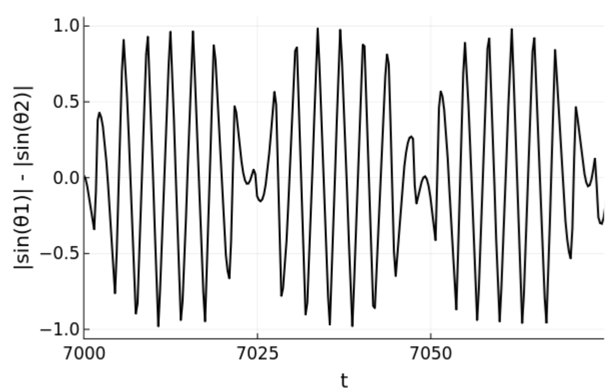

(f) $\max(|\sin(\theta_1)| - |\sin(\theta_2)|) \sim 1.0$, $\frac{2}{L} = \frac{2}{5.0} \approx 0.4$

Figure 3.19: For analytical comparison with the experimental data in Fig. 3.18, we consider an initial condition $(0.08, 0.8, 0.0, -1.1)$, which exhibits quasi-periodic motion for $(K, L) = (2.0, 1.5)$. As we vary L to 1.5, 3.0, and 5.0, the system becomes desynchronized, as indicated by the left column of figures showing the sine (red) and cosine (black) of angles between the rotors. This is analytically verified by comparing the maximum amplitude of $|\sin(\theta_1)| - |\sin(\theta_2)|$ with the synchronization condition for each case (right column). The values fall well below the synchronization threshold of $\frac{2}{L}$ Eq. (3.38), indicating synchronized motion for the first two cases. However, when $L = 5.0$ the maximum amplitude exceeds the synchronization threshold of $\frac{2}{5.0} = 0.4$, indicating unsynchronized quasi-periodic motion, where the rotors act independently of each other.

Thus far, our model has successfully replicated all previously discovered results, notably showcasing counter-rotating synchronization. Before concluding this chapter, we introduce several novel features of the current model that are yet to be thoroughly understood. However, we embark on this exploration to pave the way for further studies and investigations.

3.7 Libration Limit

As depicted in Figs. 3.16, 3.17, the cosine of angles does not span over the range $[-1,1]$, instead cutting off in between. We refer to this reciprocating motion as libration and define the maximum amplitude of oscillation as the libration limit. It's important to emphasize that we have yet to fully comprehend this behavior, but our exploration lays the groundwork for understanding this phenomenon. Furthermore, the insights gained in the upcoming subsections can be generalized to all potentials of the form $\frac{1-e^{-Kr^n}}{r}$ with $n > 2$.

3.7.1 Connection with Synchronization

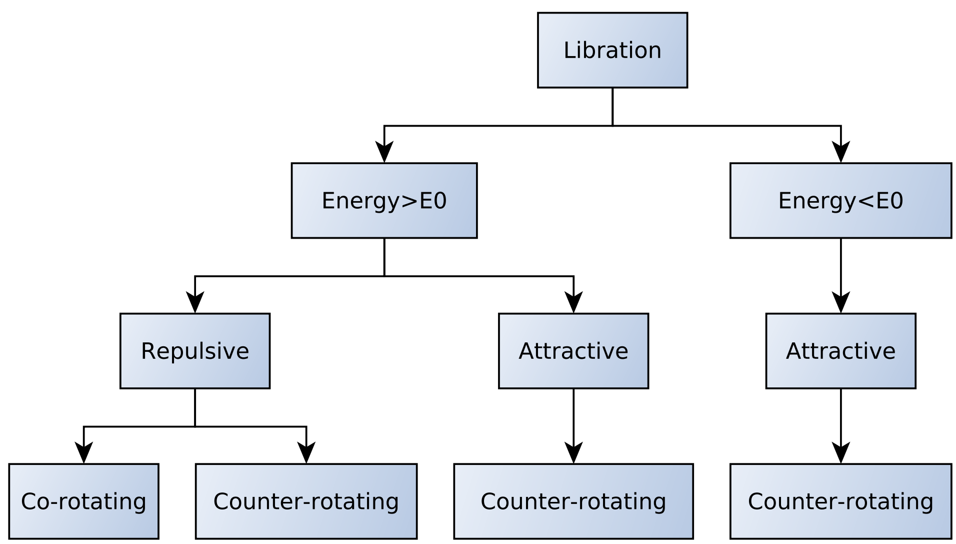

Figure 3.20: Flowchart illustrating the characteristics of libration, with the bottom nodes indicating the type of synchronized motion.

In this subsection, we explore synchronization in librated motions. When the energy of the system E surpasses a certain threshold E_0, two types of librated motion occur: one due to the attractive nature and the other due to the repulsive nature of the force. Conversely, when the energy falls below the threshold, only attractive force libration is observed, particularly around the fixed points identified earlier. The flowchart in Fig. 3.20 illustrates this information for two energy levels of the system: $E = 0.500$ and $E = 0.063$. For the librated motion due to attraction, only counter-rotating synchronization is observed while repulsive one shows both co- and counter-rotating synchronization. Additionally, we attempt to analytically determine the r [5] for these energy levels and investigate if we can establish a bound for the libration limit.

Case I: $E = 0.500$

We aim to determine the corresponding value of r by setting the potential V_0 equal to the energy E. Initially, we fix the maximum potential to $V_0(r) = 0.500$ and derive the following equation:

$$\begin{aligned} V_0 &= E \\ \frac{1-e^{-Kr^3}}{r} &= E \qquad (3.39) \\ \frac{1}{r} - \left(\frac{1-Kr^3+O(r^6)}{r}\right) &= E \\ r^2 &= \frac{E}{K}. \qquad (3.40) \end{aligned}$$

For $E = 0.5$ and $K = 2.0$, the calculated value of r is 0.5. Subsequently, we employ numerical methods to solve Eq. (3.39) utilizing the expression $r(\theta_1, \theta_2)$ Eq. (3.6) to determine the (θ_1, θ_2). Fig. 3.29 displays two mirror contours corresponding to two distinct r values. The inner contour corresponds to $r = 0.5397$, representing an attractive force, while the outer contour corresponds to $r \approx 2.00$, indicating a repulsive force.

Despite our efforts, Eq. (3.40) only yields one value of r, leading us to conclude with the first truncation in the potential, the repulsive r value cannot be determined, and including the next order results in solving a cumbersome fifth-order polynomial, prompting us to proceed with the next case.

[5] corresponding distance between the two ends of the camphor ribbons

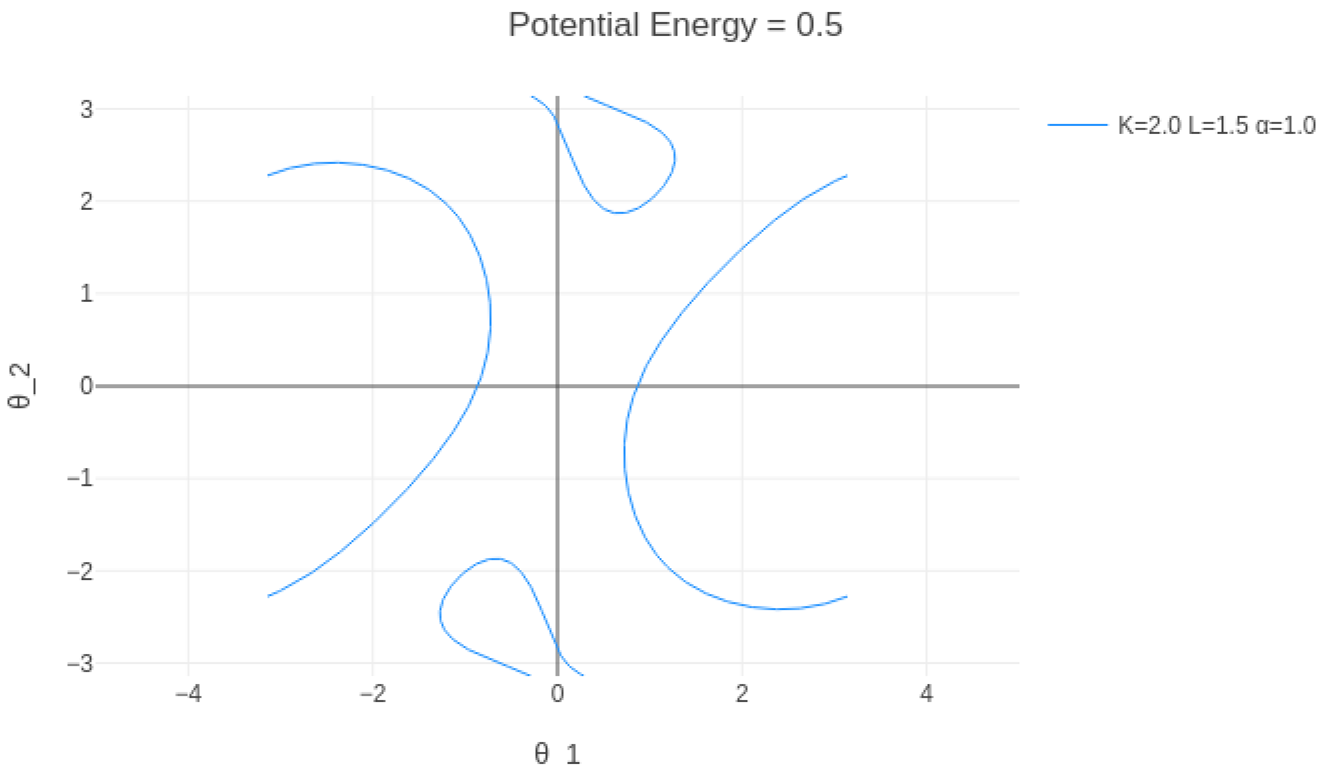

Figure 3.21: contours satisfying $V_0 = 0.5$,inner one corresponds to $r = 0.5397$ (attractive) while outer ones correspond to $r \approx 2.00$ (repulsive).

Case II: $E = 0.063$

To address the aforementioned issue, we examine small values of E where the repulsive contour is absent. We select an energy level of $E = 0.063$ and numerically determine the set of values for (θ_1, θ_2) as depicted in Fig. 3.22.

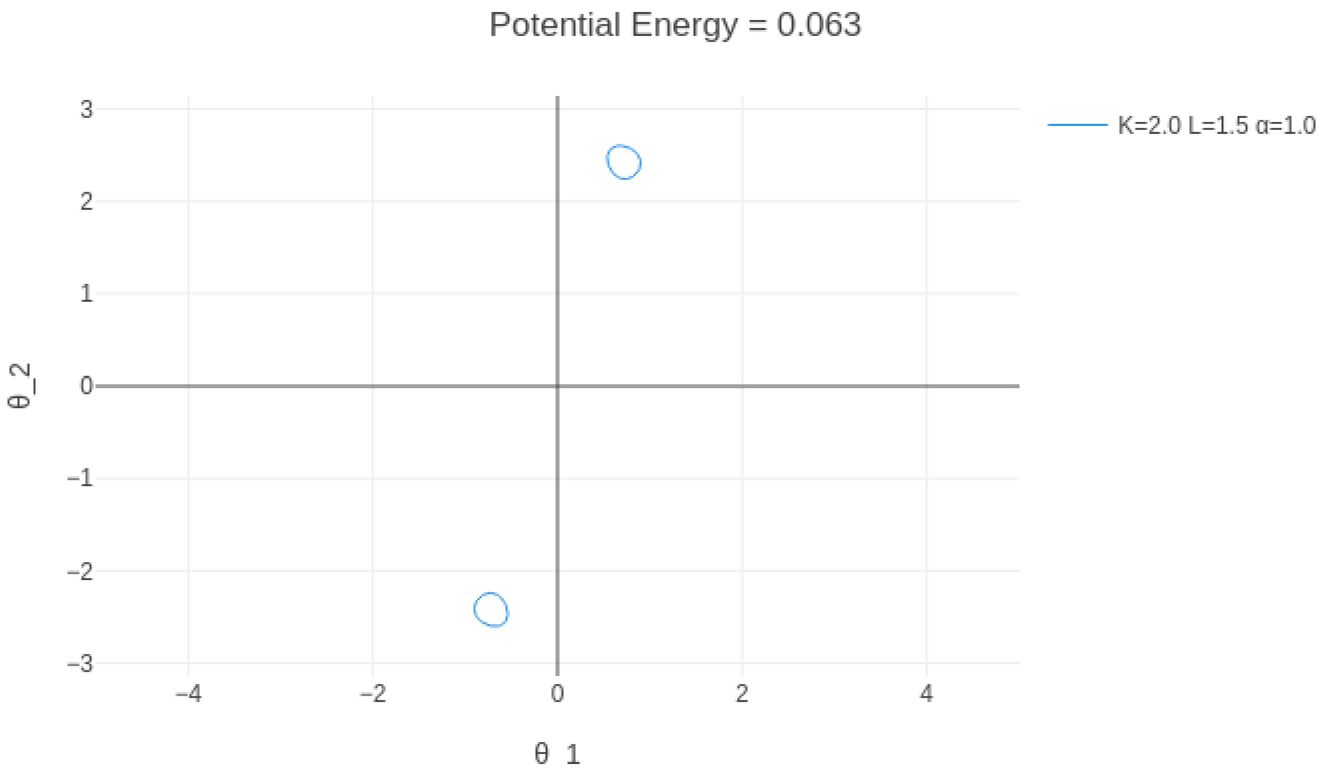

Figure 3.22: contours satisfying $V_0 = 0.063$,inner one corresponds to $r = 0.1779$ (attractive).

Analytically, from Eq. (3.40), $r^2 = \frac{0.063}{2.0}$ and $r \approx 0.1775$ which aligns with the numerical result. Now r is function of (θ_1, θ_2) by Eq. (3.6) and utilizing Eq. (3.40), we can express it as:

$$
\begin{aligned}
r^2 &= \alpha^2 + 1 + L^2 - 2L(\alpha\cos\theta_1 - \cos\theta_2) - 2\alpha\cos(\theta_1 - \theta_2) \\
\frac{E}{K} &= \alpha^2 + 1 + L^2 - 2L(\alpha\cos\theta_1 - \cos\theta_2) - 2\alpha\cos(\theta_1 - \theta_2).
\end{aligned} \tag{3.41}
$$

The above equation forms a transcendental equation of two variables. Unless we convert it into a function of a single variable with a relation between $\theta_1$and θ_2 that matches the libration limit, further analysis is not feasible. Additionally, initial conditions also influence the determination of this limit. While the analytical libration limit has not been explored yet, we are able to identify a bounded region, as illustrated in Fig. 3.23, by considering an initial condition corresponding to this particular energy $E = 0.063$.

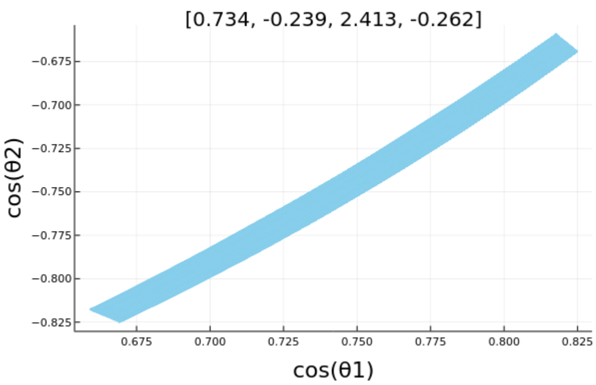

(a) Cosine of angles of two rotors.

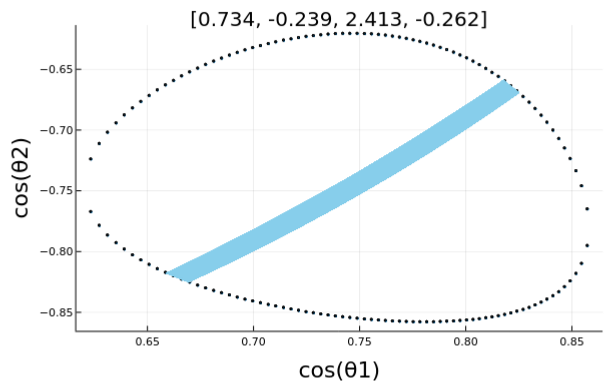

(b) Set of numerically computed (θ_1, θ_2) - (black dots) satisfying Eq. (3.41) which bounds the cosine of angle of rotors.

Figure 3.23: Synchronization at $E = 0.06305$ and corresponding $r = 0.17793$; initial condition $(0.734, -0.239, 2.413, -0.262)$ corresponds to potential energy, 0.00026.

With this, we wrap up our discussion on the model, shifting our focus on tools used and future prospects.

Chapter 4

Interactive Visualization

This dissertation heavily relies on computational power, and due credit is given to the tools that facilitated the generation of results. The entirety of the outcomes was crafted to be interactive, allowing for a dynamic analysis of parameter changes. This approach not only enhances the engagement in the study but also aids in building an intuitive understanding of the model.

Non-linear differential equation were solved using Julia's DifferentialEquations.jl Rackauckas & Nie (2017) package. The algorithm utilized was RK4 with a constant time step of 10^{-4}. Given the conservative nature of the system under consideration, the validity of Fig. (3.11-3.13) is confirmed by time series plots of energy. An illustrative energy series plot, corresponding to initial condition close to $(0,0,\pi,0)$ is presented in Fig. (4.1).

Additionally, all the symbolic calculations and simplifications were cross checked using Maxima[1].

4.1 Interaction

The conventional approach of creating simulated videos and compiling figures for different parameter sets demands considerable time and resources, particularly when studying unfamiliar systems that require thorough familiarization. To foster intuitive comprehension and familiarity with the system, all code components were crafted to enable user interaction. This design empowers individuals without prior system knowledge to effectively engage and glean insights into the effects of parameter adjustments and diverse initial conditions. These user-friendly visual interactions are facilitated through two distinct methods.

1. **Dynamic Parameter Adjustments:** All visualizations and images in this dissertation were generated using the interactive Pluto.jl [2] notebook environment, coupled with the Plotly.jl[3] backend. This setup facilitated the incorporation of interactive sliders and fields, as depicted in Fig. (4.2), enabling real-time parameter adjustments and enhancing the exploration and comprehension of the model.

[1] Manipulator of symbolic and numerical expressions written in LISP - homepage
[2] A package that creates reactive and reproducible notebooks for Julia - homepage
[3] A graphic library in Julia - homepage

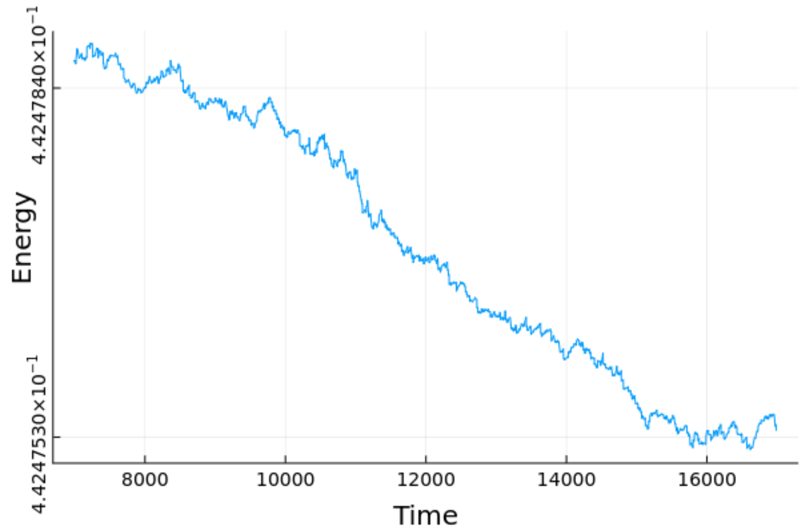

Figure 4.1: Energy calculated at each numerically integrated point from an initial condition taken close to $(0,0,\pi,0)$, demonstrating energy conservation up to six decimal places.

2. **Time Evolution Visualization**: To replicate the experimentalist's perspective, users were empowered to position the camphor ribbon through successive clicks, as illustrated in Fig. (4.3). This functionality was achieved by implementing instant step-by-step integration, inspired by a demo from DynamicalSystems.jl Datseris (2018), and initializing these integrated variables as observables, GLMakie.jl[4] auto updates the plot in real-time, enabling simulations with live adjustments to initial conditions.

It is noteworthy that all the tools employed in this study respect user privacy and adhere to the principles of **Free/Libre/Open Source Software**, fostering the joy of computing. This section concludes with an emphasis on the use of these tools and paves the way for the final remarks on the overall study.

[4]One of the backend for Makie.jl that uses GPU via OpenGL for fast animations

Abstract

1. Fix energy $\mathcal{H}$ and then potential energy V_0 of the system such that $\mathcal{H} - V_0 \geq 0$
2. Find (θ_1, θ_2) corresponding to above conditions from $r(\theta_1, \theta_2)$ constrain
3. Find p_1 by fixing p_2

$$p_1^2 = 2\alpha^2(\mathcal{H} - V_0 - \frac{p_2^2}{2})$$

4. Iterate over V_0 and make a list of initial condtions for corresponding energy

Parameters

Potential order, n = (3)

Exponential factor, K = 2.0

Length between 2 rotors L = 1.5

α - rotor arm parameter = 1.0

For Evolution

Total Energy= 0.5

Potential Energy= 0.4

p2 = -0.01

Potential Counters

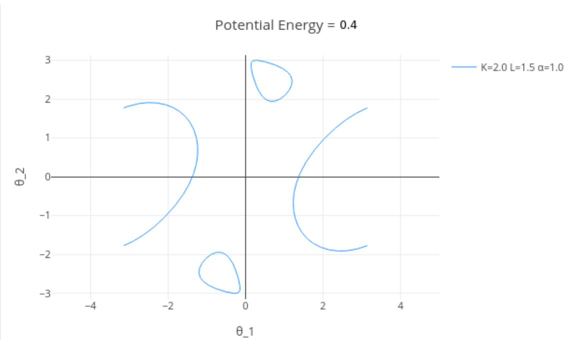


```
let
    f(x,y) = x^2+y^2-3
    r(x,y)= sqrt((α^2+1+l^2-2*l*(α*cos(x)-cos(y))-2*α*cos(x-y)));
    hv(x,y)=-p_energy+((1-exp(-K*(r(x,y)+ξ)^n))/(r(x,y)+ξ))

    p = plot_implicit(ImplicitFunction(hv); xlims = (-pi,pi), title="Potential Energy
    = 0.063", lab = "K=$(k) L=$(l) α=$(α)", xaxis_title="θ_1", yaxis_title="θ_2",
    lw=2)
    add_plotly_listener!(p, "plotly_click", "
    (e) => {
        let dt = e.points[0]
        PLOT.value = [dt.x, dt.y]
        PLOT.dispatchEvent(new CustomEvent('input'))
    }
    ")
    @bind point p
end
```

```
[0.779493, 1.88524]
```

```
[0.779493, 0.447102, 1.88524, -0.01]
```

```
@show u0
```

```
u0 = [0.7794929146766663, 0.4471017781221631, 1.8852415084838867, -0.01]
```

Figure 4.2: Interactive script allowing users to select initial conditions by clicking on potential contours. Users can vary initial total energy, potential energy, and conjugate momentums using input fields, while also adjusting the order of the Coulomb-Yukawa potential using a slider.

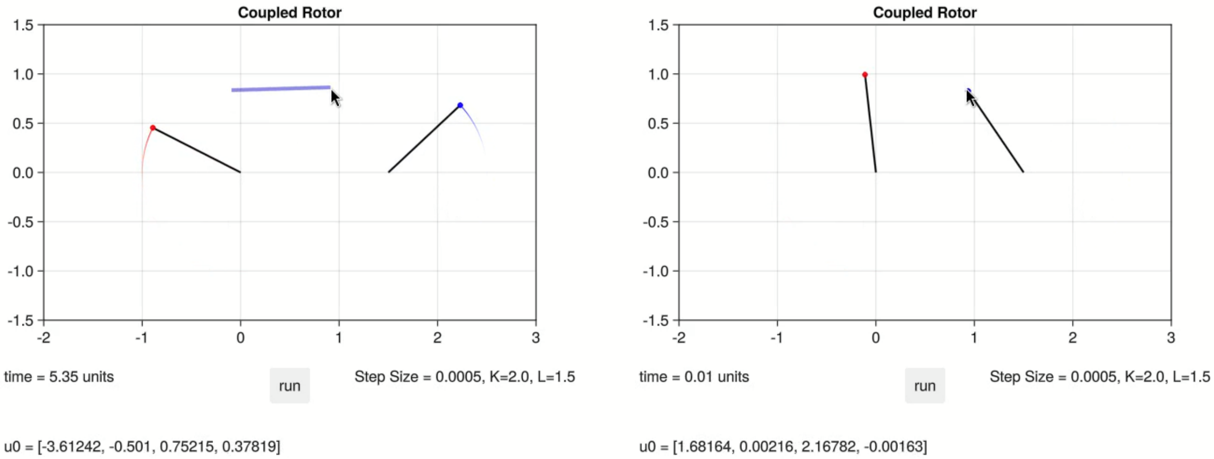

(a) Two consecutive frames of simulation demonstrating rotor response to user clicks and the subsequent alteration of their initial conditions (video).

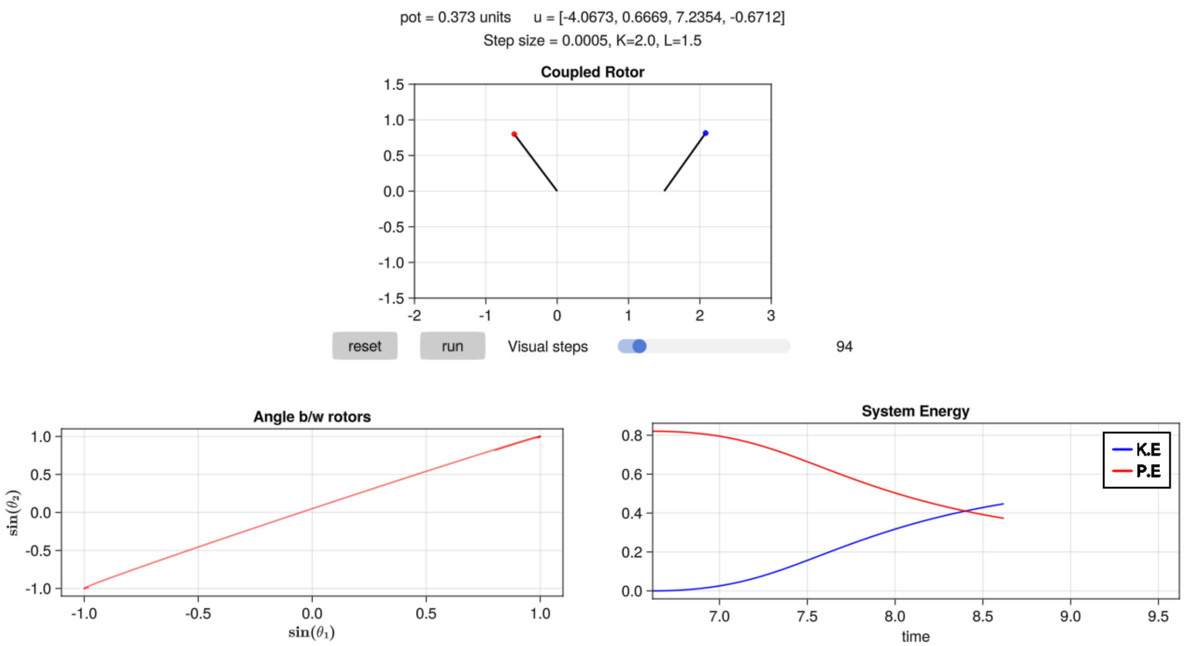

(b) An enhanced interactive simulation featuring two live secondary plots showcasing the relationship between $\sin\theta_1$ and $\sin\theta_2$, as well as the kinetic and potential energy of the system plotted against time (video).

Figure 4.3: Screenshots of interactive simulation.

Chapter 5

Outlook

5.1 Summary of Main Results

Fixed points

Our primary motivation for remodeling stemmed from the inability to capture the oscillatory behavior observed in the experimental video around $(S4)$ represented in Fig. 3.6b. After thorough exploration (see Subsec. 3.1.1), we successfully addressed this challenge by employing a Coulomb-Yukawa type potential, represented by

$$V = \frac{1 - e^{-Kr^n}}{r}.$$

The fixed points identified within the system were categorized as centers, confirming the behavior as small oscillations.

Removal of Singularity

Another obstacle we encountered was the inability to conduct stability analysis due to the vanishing elements in the Jacobian matrix. Through extensive exploration (see Subsec. 3.1.1), we resolved this issue by setting n to be strictly greater than 2 in the Yukawa-Coulomb potential. It's noteworthy that this potential not only exhibited oscillatory behavior around fixed points due to its attractive and repulsive nature but also eliminated the singularity observed in the Jacobian matrix elements (see Sec. 3.5).

Aspects of Synchronization

Our investigation also delved into synchronization phenomena observed among rotor states, which exhibited co- and counter-rotation. We successfully verified the analytical conditions for synchronization, both numerically (see Sec. 3.6) and through comparison with previously published experimental results, shown in Fig. 3.19. This further emphasizes the validity of the model under study.

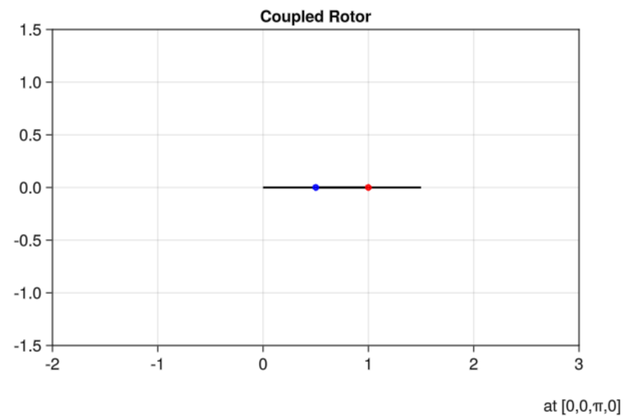

Figure 5.1: At the initial condition $(0,0,\pi,0)$, rotors being on top of each other.

Libration

Furthermore, our study revealed observations of libration (see Sec. 3.7) in the newly modeled potential. By examining system at fixed energy, we depicted possible synchronization characteristics in Fig. 3.20 and numerically determined a total bound for such synchronized libration (see Fig. 3.23).

5.2 Limitations of Current Model

Conservativeness

In the studied camphor model, one of the dominant source of motion is the surface tension gradient resulting from the dispersion of camphor molecules on the water surface. This feature introduces dissipation into the system, rendering it non-conservative, but we have modeled the system as conservative one without including mass reduction factor. Additionally, it's important to note that the pressure gradient resulting from sublimation also influences the motion of camphor ribbons.

Reduced Degree of Freedom

When two ribbons are pivoted on the surface of water, an additional degree of freedom arises from the possibility of lateral translation instead of being confined to a 2-D plane. This lateral motion becomes apparent in the configuration $(0,0,\pi,0)$ depicted in Fig. 5.1. The introduction of this extra degree of freedom is essential for capturing the realistic behavior of the system, allowing for lateral movement that significantly influences the overall dynamics of the coupled ribbons.

5.3 Future Prospects

Libration Limit

Despite numerically determining the entire bound for libration motion for a specific energy value $E = 0.063$ in Fig. 3.23, an exact analytical limit for such motion has not yet been explored. Investigating this further could enhance our understanding of the potential's characteristics.

Improvements in Modeling

The possibilities for remodeling the current system are virtually endless, offering opportunities to capture additional complexities and enhance its realism. One avenue for improvement could involve incorporating mass factors into the model. Accounting for the mass distribution of camphor ribbons could influence their motion dynamics, providing a more accurate representation of their behavior on the water's surface.

Introducing extra degrees of freedom is another promising direction for remodeling. The current model assumes certain constraints, but allowing for additional degrees of freedom could account for lateral translations, vibrations, or other motions that may impact the overall system dynamics.

Furthermore, considering the dynamics of **diffusion** along with the particle dynamics could add another layer of realism. Diffusion processes on the water's surface could interact with the motion of camphor ribbons, leading to more intricate and realistic behaviors. This would be particularly relevant when studying the **dissipative aspects** of the system.

References

Chen, W., Vermaak, I., & Viljoen, A. (2013). Camphor–a fumigant during the black death and a coveted fragrant wood in ancient egypt and babylon–a review. Molecules (Basel, Switzerland), 18, 5434–54. 10

Cruz, J.-M., Díaz-Hernández, O., Castañeda-Jonapá, A., Morales-Padrón, G., Estudillo, A., & Salgado-García, R. (2024). Active chiral dynamics and boundary accumulation phenomenon in confined camphor particles. Soft Matter, 20(6), 1199–1209. 16

Datseris, G. (2018). Dynamicalsystems.jl: A julia software library for chaos and nonlinear dynamics. J. Open Source Softw., 3(23), 598. 44

Hayashima, Y., Nagayama, M., & Nakata, S. (2001). A camphor grain oscillates while breaking symmetry. The Journal of Physical Chemistry B, 105(22), 5353–5357. 13, 15

Jain, R., Sharma, J., Tiwari, I., Gadre, S. D., Kumarasamy, S., Parmananda, P., & Prasad, A. (2022). Generation of aperiodic motion due to sporadic collisions of camphor ribbons. Physical Review E, 106(2), 024201. viii, 9, 15, 16, 32

Jain, R., Sharma, J., Tiwari, I., Gadre, S. D., Kumarasamy, S., Parmananda, P., & Prasad, A. (2023). In-phase and mixed-phase measure synchronization of camphor rotors. Physical Review E, 108(2), 024217. vii, viii, ix, 9, 15, 16, 32, 35, 36

Kaiser, A., Popowa, K., Wensink, H. H., & Löwen, H. (2013). Capturing self-propelled particles in a moving microwedge. Physical Review E, 88(2), 022311. 16

Kitahata, H., Hiromatsu, S.-i., Doi, Y., Nakata, S., & Rafiqul Islam, M. (2004). Self-motion of a camphor disk coupled with convection. Physical Chemistry Chemical Physics, 6(9), 2409. 11

Koyano, Y., Gryciuk, M., Skrobanska, P., Malecki, M., Sumino, Y., Kitahata, H., & Gorecki, J. (2017). Relationship between the size of a camphor-driven rotor and its angular velocity. Physical Review E, 96(1), 012609. 13

Lorenz, E. N. (1963). Deterministic nonperiodic flow. J. Atmos. Sci., 20, 130–141. 1

Mann, J., Davidson, R. S., Hobbs, J. B., Banthorpe, D., Harborne, J. B., et al. (1994). Natural products: their chemistry and biological significance. Longman Scientific & Technical. 10

Nakata, S., Doi, Y., & Kitahata, H. (2005). Synchronized sailing of two camphor boats in polygonal chambers. The Journal of Physical Chemistry B, 109(5), 1798–1802. 15

Nakata, S., Kohira, M. I., & Hayashima, Y. (2000). Mode selection of a camphor boat in a dual-circle canal. Chemical Physics Letters, 322(5), 419–423. 15

Nakata, S., Yamamoto, H., Koyano, Y., Yamanaka, O., Sumino, Y., Suematsu, N. J., Kitahata, H., Skrobanska, P., & Gorecki, J. (2016). Selection of the rotation direction for a camphor disk resulting from chiral asymmetry of a water chamber. The Journal of Physical Chemistry B, 120(34), 9166–9172. viii, 13, 14

Nakata Satoshi, I. Y. & Ose (1997). Self-rotation of a camphor scraping on water: Newinsight into the old problem. Langmuir, 13(16), 4454–4458. viii, 10, 11, 13

Rackauckas, C. & Nie, Q. (2017). Differentialequations.jl – a performant and feature-rich ecosystem for solving differential equations in julia. Journal of Open Research Software, 5(1). 43

Sharma, J., Tiwari, I., Das, D., Parmananda, P., Akella, V. S., & Pimienta, V. (2019). Rotational synchronization of camphor ribbons. Physical Review E, 99(1), 012204. viii, 9, 15, 16

Sharma, J., Tiwari, I., Das, D., Parmananda, P., & Pimienta, V. (2020). Rotational synchronization of camphor ribbons in different geometries. Physical Review E, 101(5), 052202. viii, 9, 16

Strogatz, S. H. (2015). Nonlinear dynamics and chaos. With applications to physics, biology, chemistry, and engineering. Boulder, CO: Westview Press, 2nd edition edition. 1

Suematsu, N. J., Ikura, Y., Nagayama, M., Kitahata, H., Kawagishi, N., Murakami, M., & Nakata, S. (2010). Mode-switching of the self-motion of a camphor boat depending on the diffusion distance of camphor molecules. The Journal of Physical Chemistry C, 114(21), 9876–9882. 12, 14

Suematsu, N. J., Sasaki, T., Nakata, S., & Kitahata, H. (2014). Quantitative estimation of the parameters for self-motion driven by difference in surface tension. Langmuir, 30(27), 8101–8108. viii, 10, 11, 12

Suematsu, N. J., Tateno, K., Nakata, S., & Nishimori, H. (2015). Synchronized intermittent motion induced by the interaction between camphor disks. Journal of the Physical Society of Japan, 84(3), 034802. 15

Appendix A

Source Code - Animation

Based on the Makie.jl demo found at the provided URL[1], the rotor behavior was enhanced to dynamically respond to user clicks, allowing for adjustment of their initial conditions. Additionally, two miniature plots were added below, displaying the relationship between $\sin\theta_1$ and $\sin\theta_2$ of both rotors. Another miniature plot illustrates the kinetic and potential energy of the coupled rotor system.

[1] https://gist.githubusercontent.com/Datseris/4b9d25a3ddb3936d3b83d3037f8188dd/raw/6e43086901c42ad45243db7c9f24d5fcda4f16fb/makie_tutorial.jl

```
## Making animated and interactive scientific
## visualizations in Makie.jl - Based on
↪  Datseris's
## guide, linked in footnotes of Appendix

# 1. Initialize simulation in a stepping manner
# 2. Initialize the `Observable`s of the
↪  animation
# 3. Plot the `Observable`s and any other
↪  static elements
# 4. Create the "animation stepping function"
# 5. Test it
# 6. Save animations to videos (optional)
# 7. Interactive application

using DynamicalSystems
using OrdinaryDiffEq, DifferentialEquations
using GLMakie
using DataStructures: CircularBuffer

# %% 1. Initialize simulation in a stepping
↪  manner
# --------------------------------

# initial conditions
u0=[-1.38,0.,4.57,0.0]
t0 = 0.00
step_size = 0.0005

# order of r in potential
n=3

# parameters
K = 2.0 #exponential factor
L = 1.5 #seperation distance
α = 1.0
ξ = 0.0
A = 1.0
B = 0.0

params = [K, L, α, ξ, A, B]

# governing diffeq
function rotor_2(u, params, t)
  θ1,p1,θ2,p2 = u
  K,L,α,ξ,A,B = params
  r=sqrt(abs(α^2+1+L^2-2*L*(α*cos(θ1)-cos(θ2))-
↪  2*α*cos(θ1-θ2)));
  r=r+ξ
  # necessary factors
  v0     = (1-exp(-K*r^n))/r
  pv0_r  =
↪  -exp(-K*r^n)*(-1-n*K*r^n+exp(K*r^n))/(r^2)
  # pv02_r = -2*exp(-2*K*r)*(1+K*r)/(r^3)
  pr_θ1  = (α*(sin(θ1-θ2)+L*sin(θ1)))/r
```

```
  pr_θ2  = (α*sin(θ2-θ1) -L*sin(θ2)) /r
  factor = ( ((1/α^2)+1)*v0*B^2 +
↪  (B*((-p1/α^2)+p2)+A) ) * pv0_r

  du1 = (p1-B*v0)/(α^2)
  du2 = -factor*pr_θ1
  du3 = (p2+B*v0)
  du4 = -factor*pr_θ2

  return SVector{4}(du1, du2, du3, du4)
end

# algorithm
diffeq = (alg = RK4(), reltol = 1e-10, abstol =
↪  1e-10 , atol=1e-10,rtol=1e-10, adaptive =
↪  false, dt = step_size)

# initializing integrator
rotor_system =  CoupledODEs(rotor_2, u0,
↪  params; diffeq, t0 = 0.0)
integ = rotor_system.integ

# constant step wise results
function xycoords(state)
  θ1 = state[1]
  θ2 = state[3]
  x1 = α*cos(θ1)
  y1 = α*sin(θ1)
  x2 = L + cos(θ2)
  y2 = sin(θ2)
  return x1,x2,y1,y2
end

function xytime(t)
 return "$(t) sec"
end

# combined `integ` = integrator. `step!(integ)`
↪  progresses stepwise
function progress_for_one_step!(integ)
  step!(integ)
  return xycoords(integ)
end

# %% 2. Initialize the `Observable`s of the
↪  animation
# --------------------------------

# animated elements: balls as ribbon ends # and
↪  rods as ribbons
x1,x2,y1,y2 = xycoords(u0)
rod1   = Observable([Point2f(0, 0), Point2f(x1,
↪  y1)])
rod2   = Observable([Point2f(L, 0), Point2f(x2,
↪  y2)])
```

```julia
balls = Observable([Point2f(x1, y1),
 ↪  Point2f(x2, y2)])

# observable for the tail
# circular buffer = trailing animated residue
tail2 = 150 # length in `dt`
traj2 = CircularBuffer{Point2f}(tail2)
fill!(traj2, Point2f(x2, y2)) # add correct
 ↪  values to the circular buffer
traj2 = Observable(traj2) # make it an
 ↪  observable

tail1 = 150
traj1 = CircularBuffer{Point2f}(tail1)
fill!(traj1, Point2f(x1, y1))
traj1 = Observable(traj1)

# dynamic upadation of time, state
t_value = Observable(0.0)
i_value = Observable(u0)

# %% 3. Plot the `Observable`s and any other
 ↪  static elements
# ------------------------------

# initialie a figure
fig = Figure(); display(fig)
ax = Axis(fig[1,1])

# plot the observables, ribbon and ribbon ends
lines!(ax, rod1; linewidth = 2, color = :black)
lines!(ax, rod2; linewidth = 2, color = :black)
scatter!(ax, balls; marker = :circle,
 ↪  strokewidth = 2,
  strokecolor = [:red,:blue],
  color = [:red,:blue], markersize = [1, 1]
)

# trajectory with a nice fadeout color
c2 = to_color(:blue)
tailcol2 = [RGBAf(c2.r, c2.g, c2.b,
 ↪  (i/tail2)^2) for i in 1:tail2]
lines!(ax, traj2; linewidth = 1, color =
 ↪  tailcol2)

c1 = to_color(:red)
tailcol1 = [RGBAf(c1.r, c1.g, c1.b,
 ↪  (i/tail2)^2) for i in 1:tail1]
lines!(ax, traj1; linewidth = 1, color =
 ↪  tailcol1)

# static elements
ax.title = "Coupled Rotor at $(u0)"
ax.aspect = DataAspect()
xlims!(ax, -3, +3)
ylims!(ax, -1.5, 1.5)

# %% 4. Create the "animation stepping function"
# ---------------------------------

# combining all previously defined observables
 ↪  with integrator
function animstep!(integ, rod1, rod2, balls,
 ↪  traj1, traj2)
  x1,x2,y1,y2 = progress_for_one_step!(integ)
  rod1[] = [Point2f(0, 0), Point2f(x1, y1)]
  rod2[] = [Point2f(L, 0), Point2f(x2, y2)]
  balls[] = [Point2f(x1, y1), Point2f(x2, y2)]
  t_value[]=integ.t;
  i_value[]=integ.u;
  push!(traj1[], Point2f(x1, y1))
  push!(traj2[], Point2f(x2, y2))
  # triggering updates
  traj1[] = traj1[];
  traj2[] = traj2[];
end

# %% 5. Testing and  combining as whole function
# --------------------------------

for i in 1:100
  animstep!(integ, rod1, rod2, balls, traj1,
 ↪  traj2)
  sleep(0.001)
end

function rotor_fig(u0)
  params = [K, L, α, ξ, A, B]

  ## diffeq = (alg = Vern7(), reltol = 1e-8,
 ↪  abstol = 1e-8 , atol=1e-8,rtol=1e-8,
 ↪  adaptive = false, dt = 0.5)
  rotor_system =  CoupledODEs(rotor_2, u0,
 ↪  params; diffeq, t0 = 0.0)
  integ = rotor_system.integ

  x1,x2,y1,y2 = xycoords(u0)
  rod1   = Observable([Point2f(0, 0),
 ↪  Point2f(x1, y1)])
  rod2   = Observable([Point2f(L, 0),
 ↪  Point2f(x2, y2)])
  balls = Observable([Point2f(x1, y1),
 ↪  Point2f(x2, y2)])

  tail2 = 150
  traj2 = CircularBuffer{Point2f}(tail2)
  fill!(traj2, Point2f(x2, y2))
  traj2 = Observable(traj2)

  tail1 = 150
```

```
  traj1 = CircularBuffer{Point2f}(tail1)
  fill!(traj1, Point2f(x1, y1))
  traj1 = Observable(traj1)

  t_value = Observable(0.0)
  i_value = Observable(u0)

  #fig = Figure(); display(fig)
  #ax = Axis(fig[1,1])

  fig = Figure(resolution = (1600, 800));
↪  display(fig)
  primary_layout = fig[1,:] = GridLayout()
  ax = Axis(primary_layout[2,:])

  lines!(ax, rod1; linewidth = 2, color =
↪  :black)
  lines!(ax, rod2; linewidth = 2, color =
↪  :black)
  scatter!(ax, balls; marker = :circle,
↪  strokewidth = 2,
      strokecolor = [:red,:blue],
      color = [:red,:blue], markersize = [3, 3]
  )

  # needs tailcol function
  lines!(ax, traj1; linewidth = 1, color =
↪  tailcol1)
  lines!(ax, traj2; linewidth = 1, color =
↪  tailcol2)

  #ax.title = "Coupled Rotor $(round.(u0;
↪  digits=3))"
  ax.title  = "Coupled Rotor"
  ax.aspect = DataAspect()
  xlims!(ax, -2.0, L+1.5)
  ylims!(ax, -1.5, 1.5)

  return fig, primary_layout, integ, rod1,
↪  rod2, balls, traj1, traj2
end


# final parameters that gets returned
fig, primary_layout, integ, rod1, rod2, balls,
↪  traj1, traj2 = rotor_fig(u0)


# %% 6. Save animations to videos (optional)
# ----------------------------

# fig, integ, rod1, rod2, balls, traj1, traj2 =
↪  rotor_fig(u0)
#
# lab1 = Label(fig[2, 1],
#         @lift("time =
↪  $(round($t_value,digits=5)) units"),
#         halign=:left,
#         tellheight= false,
#         tellwidth = false,
#         valign = :top)
#
# lab3 = Label(fig[2, 1],
#         @lift("u0 =
↪  $(round.($i_value,digits=5))"),
#         halign=:left,
#         tellheight= false,
#         tellwidth = false,
#         valign = :bottom)
#
# lab2 = Label(fig[2, 1],
#        "Step Size = $(step_size), K=$(K),
↪  L=$(L)",
#        halign=:right,
#        tellheight= false,
#        tellwidth = false,
#        valign = :top)
#
# Label(fig[2,1],"$(u0)",tellwidth=false)



# %% 7. Interactive application
# ------------------------

# %% 7.1 plot static buttons, info, subplots

# creating buttons run/stop, visual steps
fig, primary_layout, integ, rod1, rod2, balls,
↪  traj1, traj2 = rotor_fig(u0)
    control_layout = primary_layout[3,:] =
↪  GridLayout(tellheight = false, tellwidth =
↪  false)
    height = 30
    resetbutton = Button(control_layout[1,1];
        label = "reset", buttoncolor =
↪  RGBf(0.8, 0.8, 0.8),
        height, width = 70
    )
    runbutton = Button(control_layout[1,2];
↪  label = "run",
        buttoncolor = RGBf(0.8, 0.8, 0.8),
↪  height, width = 70
    )
    slidergrid = SliderGrid(control_layout[1,3],
        (label = "Visual steps", range =
↪  1:1000, startvalue = 10, height, width=200)
    )

# live info of rotor states
```

```
info_layout = primary_layout[0,:] =
 ↪  GridLayout(tellheight = true, tellwidth =
 ↪  false)
lab1 = Label(info_layout[1, 1],)
lab1.text[]="time =
 ↪  "*string(round(t_value[],digits=5))* "
 ↪  units"
lab3 = Label(info_layout[1, 2],)
lab3.text[]="u =
 ↪  "*string(round.(i_value[],digits=4))

# labels for initial conditions
infostatic_layout = primary_layout[1,:] =
 ↪  GridLayout(tellheight = true, tellwidth =
 ↪  false)
lab2 = Label(infostatic_layout[1, 1],
        "Step size = $(step_size), K=$(K),
 ↪  L=$(L)",
        tellheight= true,
        )

rowsize!(primary_layout, 0, 0)
rowsize!(primary_layout,1, 0)
rowsize!(primary_layout,2, Relative(0.9))
rowsize!(primary_layout, 3, 0)

# subplot
# 1. sine of angles between rotors
time_layout = fig[2,:] = GridLayout()
ax_time = Axis(time_layout[1,1];
xlabel = L"\mathbf{\sin(θ_1)}",
ylabel = L"\mathbf{\sin(θ_2)}",
alignmode=Outside(20),
title="Angle b/w rotors",
aspect=AxisAspect(3)
)

# subplot
# 2. system energy
ax_energy = Axis(time_layout[1,2],
title="System Energy (K.E - blue) (P.E - red)",
xlabel="Time",
alignmode=Outside(20),
aspect=AxisAspect(3)
)

# combined sub plots
rowsize!(fig.layout, 2, Relative(.45))

# initialization for kinetic energy
k_energy(p)  =(p[2]^2/(2*α^2))+(p[4]^2/2)

# instead of k_energy if distance is required
# function k_energy(p)
#   θ1,pθ1,θ2,pθ2 = p
#   K, L, α, ξ, A, B = params
#   # fma(a,b,c) = a*b + c
#   (s1,c1)  = α.*sincos(θ1)
#   (s2, c2) = sincos(θ2)
#   r = let
#    a = fma(s1, s2, 1)
#    b = fma(c1, c2, a)
#    c = fma(L, c1 - c2, b)
#    d = fma(L, L, -2*c)
#    (sqrt ∘ abs)(d+3.0+α^2)+ξ
#   end
#   return r
# end

# initialization for potential energy
function pot_energy(p)
  θ1,pθ1,θ2,pθ2 = p
  K, L, α, ξ, A, B = params

  # viable fucntion fma(a,b,c) = a*b + c
  (s1,c1)  = α.*sincos(θ1)
  (s2, c2) = sincos(θ2)
  r = let
    a = fma(s1, s2, 1)
    b = fma(c1, c2, a)
    c = fma(L, c1 - c2, b)
    d = fma(L, L, -2*c)
    (sqrt ∘ abs)(d+3.0+α^2)+ξ
  end
  return (1-exp(-K*r^n))/r
end

# %% 7.2 Adding functionality
# live update of time, state vector observables
tt = Observable([0.0]) # Time axis
r1 = Observable([sin.(i_value[][1])])
r2 = Observable([sin.(i_value[][3])])
# live update of energy subplot observables
e1 = Observable([k_energy(i_value[])])
e2 = Observable([pot_energy(i_value[])])
lines!(ax_time, r1, r2; color =
 ↪  :red,alpha=0.6,linestyle=:solid)
# update the subplots
lines!(ax_energy, tt, e1; color = :blue,
 ↪  label="K.E")
lines!(ax_energy, tt, e2; color = :red,
 ↪  label="P.E")

# %% Run/stop based on user clicks
# observe changes into this function
isrunning = Observable(false)
on(runbutton.clicks) do clicks; isrunning[] =
 ↪  !isrunning[]; end
on(runbutton.clicks) do clicks
@async while isrunning[] # without `@async`,
 ↪  Julia "freezes" in this loop
```

```julia
  n = slidergrid.sliders[1].value[]
  # visual steps = skipping frams
  for _ in 1:slidergrid.sliders[1].value[]-1
    animstep!(integ, rod1, rod2, balls, traj1, traj2)
  end

  # update labels
  # lab1.text[]="time = "*string(round(t_value[],sigdigits=4))* " units"
  lab1.text[]="pot = "*string(round(pot_energy(i_value[]),sigdigits=4))* " units"
  lab3.text[]="u = "*string(round.(i_value[],digits=4))

  # update timeseries
  push!(tt[], integ.t)
  push!(r1[], sin.(i_value[][1]))
  push!(r2[], sin.(i_value[][3]))
  push!(e1[], k_energy(i_value[]))
  push!(e2[], pot_energy(i_value[]))
  notify.((tt, r1, r2,e1,e2))

  autolimits!(ax_time);

  t_prev = max(0, t_value[]-2.0)
  ylims!(ax_energy)
  xlims!(ax_energy, t_prev, t_value[]+1.0);
  ax_energy.xticks=0:0.5:1000;

  animstep!(integ, rod1, rod2, balls, traj1, traj2)
    # ensures computations stop if closed window.
    isopen(fig.scene) || break
    sleep(0.00001)
  end
end

## %% changing initial condition with user selection
ax = content(fig[1,1][2,1])
Makie.deactivate_interaction!(ax, :rectanglezoom)

# select_line capturing coords
lpoint = select_line(ax.scene)
todeg_1(z) = atan(z[2],z[1])
todeg_2(z) = atan(z[2],z[1]-L)

# digression function
# function ini(c1,c2)
#   r(θ1,θ2)  = sqrt(abs(α^2+1+L^2-2*L*(α*cos(θ1)-cos(θ2))-2*α*cos(θ1-θ2)));
#   t=r(c1,c2)+ξ
#   v0(r) = exp(-K*r)/r
#   return B*v0(t)
# end

# trigger
on(lpoint) do line
  # coords to angles
  θ1,θ2 = todeg_1(line[1]), todeg_2(line[2])

  #initial condition with 0 momenta
  #p = ini(θ1,θ2)
  u0 = [θ1,0.0,θ2,0.0]
  reinit!(integ, u0)

  # Reset tail and balls to new coordinates
  x1,x2,y1,y2 = xycoords(u0)
  rod1[] = [Point2f(0, 0), Point2f(x1, y1)]
  rod2[] = [Point2f(L, 0), Point2f(x2, y2)]
  balls[] = [Point2f(x1, y1), Point2f(x2, y2)]

  t_value[]=integ.t;
  i_value[]=integ.u;

  traj1[] .= fill(Point2f(x1, y1), length(traj1[]))
  traj2[] .= fill(Point2f(x2, y2), length(traj2[]))
  traj1[] = traj1[];
  traj2[] = traj2[];

  tt[] = [0.0] # Time axis
  r1[] = [sin.(i_value[][1])]
  r2[] = [sin.(i_value[][3])]

  e1[] = [k_energy(i_value[])]
  e2[] = [pot_energy(i_value[])]
  # notify all observable changes
  notify.((tt, r1, r2,e1,e2))
end
```